Draft version September 18, 2023
Typeset using LaTeX **preprint2** style in AASTeX631

X-ray Observations of the Galactic Ecosystems — A White Paper for the Hot Universe Baryon Surveyor (HUBS)

Jiang-Tao Li,[1] Zhijie Qu,[2] Shuinai Zhang,[1] Xinwen Shu,[3] Edmund Hodges-Kluck,[4] Gabriele Ponti,[5] Yakov Faerman,[6] Rui Huang,[7] Yong Zheng,[8] Joel N. Bregman,[9] G. Mark Voit,[10] Q. Daniel Wang,[11] Yijun Wang,[12] Fabrizio Nicastro,[13] Feng Yuan,[14] Robert A. Crain,[15] Taotao Fang,[16] Chong Ge,[16] Fulai Guo,[14] Luis Ho,[17] Meicun Hou,[17] Feng Huang,[16] Suoqing Ji,[14] Hui Li,[7] Miao Li,[18] Yuan Li,[19] Zhiyuan Li,[12] Teng Liu,[20] Bin Luo,[12] Guobin Mou,[21] Yingjie Peng,[17] Yu Qiu,[22] Fangzheng Shi,[14] Mouyuan Sun,[16] Carlos Vargas,[23] Aditi Vijayan,[24] Junfeng Wang,[16] Junxian Wang,[25] Tinggui Wang,[25] Jianfeng Wu,[16] Yongquan Xue,[25] Huanian Zhang,[26] Ruiyu Zhang,[27] and Yuning Zhang[7]

[1]*Purple Mountain Observatory, Chinese Academy of Sciences, 10 Yuanhua Road, Nanjing 210023, People's Republic of China*
[2]*Department of Astronomy & Astrophysics, The University of Chicago, 5640 S. Ellis Ave., Chicago, IL 60637, USA*
[3]*Department of Physics, Anhui Normal University, Wuhu 241002, People's Republic of China*
[4]*Code 662, NASA Goddard Space Flight Center, 8800 Greenbelt Rd., Greenbelt, MD 20771, USA*
[5]*Istituto Nazionale di Astrofisica, Osservatorio Astronomico di Brera, via E. Bianchi 46, 23807 Merate (LC), Italy*
[6]*Astronomy Department, University of Washington, Seattle, WA 98195, USA*
[7]*Department of Astronomy, Tsinghua University, Beijing 100084, People's Republic of China*
[8]*Rensselaer Polytechnic Institute*
[9]*Department of Astronomy, University of Michigan, Ann Arbor, MI, 48109, USA*
[10]*Michigan State University*
[11]*Department of Astronomy, University of Massachusetts, Amherst, MA, 01003-9305*
[12]*Nanjing University*
[13]*INAF*
[14]*Shanghai Astronomical Observatory, Chinese Academy of Sciences, Shanghai 200030, People's Republic of China*
[15]*Liverpool John Moose University*
[16]*Department of Astronomy, Xiamen University, Xiamen, Fujian 361005, People's Republic of China*
[17]*Peking University*
[18]*Zhejiang University*
[19]*University of Northern Texas*
[20]*MPE*
[21]*Wuhan University*
[22]*Kavli Institute for Astronomy and Astrophysics, Peking University, Beijing 100871, PRC*
[23]*University of Arizona*
[24]*Research School of Astronomy and Astrophysics, Australian National University, Canberra ACT 2601, Australia*
[25]*University of Science and Technology of China*
[26]*Huazhong University of Science and Technology*
[27]*Henan Normal University*

ABSTRACT

Corresponding author: Jiang-Tao Li
pandataotao@gmail.com

The Hot Universe Baryon Surveyor (*HUBS*) is an X-ray mission under development, with high energy resolution, high sensitivity, and large field of view (FOV). It is optimized to detect faint X-ray emission lines from extended sources such as the hot circum-galactic medium (CGM) around local galaxies. *HUBS* will play a critical role in X-ray observations of the galactic ecosystems, which represents the galaxies and their environments co-evolving together. In this white paper, we, the *HUBS* Galactic Ecosystems science working group (SWG), will overview the scientific background of the X-ray emitting hot CGM, the key results and unresolved problems in the related fields, as well as the key characteristics and the general observational strategy of *HUBS*. We will also present a few specific science cases related to the Milky Way (MW), nearby galaxies, and AGN. These science cases will help *HUBS* or other similar future X-ray missions to finalize their instrument design and to develop key and/or reference observational projects.

Keywords: HUBS

1. SCIENTIFIC BACKGROUND: GALACTIC ECOSYSTEMS AND THE HOT CGM

The galactic ecosystems represent a combination of the galaxy and its environment which are co-evolving with each other via various types of interactions, such as galactic feedback by AGN or stellar sources, accretion of multi-phase external gas, tidal interaction between companion galaxies, and ram-pressure stripping in dense gaseous environment, etc. (e.g., Kereš et al. 2005; Veilleux et al. 2005; Vogelsberger et al. 2014; Schaye et al. 2015; Tumlinson et al. 2017). A galaxy is often embedded in the multi-phase circum-galactic medium (CGM), which is comprised of multi-phase gases, dust (e.g., Whaley et al. 2009), cosmic ray (CR), and magnetic field (e.g., Irwin et al. 2012a). The multi-phase gases in the CGM include the hot gas ($T \gtrsim 10^6$ K) emitting X-rays (e.g., Strickland et al. 2004a; Li & Wang 2013a), the transition-temperature gas ($T \sim 10^{4-6}$ K; often named "warm-hot gas") most commonly traced by UV absorption lines from high ions in the spectra of background AGN (e.g., Tumlinson et al. 2011), the $T \sim 10^{3-4}$ K cool or warm gas (named differently in different studies, hereafter "warm gas" throughout this white paper) seen in optical/UV emission lines (e.g., Rossa & Dettmar 2003; Haffner et al. 2003; Vargas et al. 2019) or absorption lines from background AGN (e.g., Wakker & Savage 2009; Werk et al. 2014), cold atomic gas often directly traced by the H I 21-cm line (e.g., Walter et al. 2008; Heald et al. 2011a; Zheng et al. 2022), and molecular gas traced by many molecular lines typically in mm-wave (cold molecular gas, e.g., Young et al. 1995; Leroy et al. 2009) or IR (warm molecular gas, e.g., Veilleux et al. 2009). This multi-phase gaseous CGM serves as a reservoir from which the galaxy acquires baryons to continue star formation (SF). It also stores the kinetic energy and chemically enriched materials deposited by various types of galactic feedback, including AGN, massive stellar wind and core collapsed supernovae (SNe) from the young stellar population, or Type Ia SNe from the old stellar population.

1.1. *The hot CGM*

Among the multi-phase gases in the CGM, the hot gas is probably the most diffuse and extended component, which often extends to the outskirts of the dark matter halo of galaxies (e.g., Fabbiano 1989; Wang 2010; Li et al. 2018; Li 2020; Bregman et al. 2018, 2022). This galactic "corona", typically distributed beyond the stellar content of the galaxies and within the virial radius of the dark matter halo, is often called the hot CGM. The hot CGM is distinguished with the same gas phase within the ISM of galaxies, or in the intra-group medium (IGrM), intra-cluster medium (ICM), or the IGM extending to much larger scales.

The exact definition of the "hot" CGM by different authors is often slightly different, but typically based on the radiative cooling curve of ionized plasma (Fig. 1; e.g., Raymond & Smith 1977; Sutherland & Dopita 1993). The radiative cooling of ionized gas in collisional ionization equilibrium (CIE) is dominated by the ionic emission lines of the most abundant elements (e.g., C, N, O, Ne, Mg, Si, S, Fe, etc.), and peaks at $T \sim 10^5$ K in the typical range of metallicities (Sutherland & Dopita 1993). For comparison, the cooling of higher-temperature gas at $T \gtrsim 10^7$ K is often dominated by the free-free emission, while at lower temperatures of $T \sim 10^{4-4.5}$ K, the Hydrogen recombination lines become more important. In this white paper, we define gas with $T \gtrsim 10^6$ K as hot gas, where the cooling is still dominated by ions, but the cooling timescale $t_{\rm cool}$ is much longer than the gas at lower temperatures. Due to its high temperature, the hot gas often tends to fill the entire space to reach pressure balance with other gas phases, so has low density. The low density, combined with the relatively low radiative cooling rate (Fig. 1), produces the much longer cooling timescale than the other gas phases. The hot CGM is thus often regarded as thermally stable, given that its radiative cooling timescale (typically $\gtrsim$ Gyr) is often much longer than the typical dynamical timescale of the global gas flows in the CGM (typically $< 1\%$ of $t_{\rm cool}$ at a given radius; e.g., Li et al. 2017a). This is clearly distinguishable from the other lower-temperature gas phases, which often cannot be thermally stable on the CGM scale.

The hot CGM could be classified into four basic types based on the origin of the gas and the primary heating mechanism:

• External gas heated mainly by the gravitational energy;

• Internal gas heated mainly by the gravitational energy;

• Internal gas heated mainly by various types of galactic feedback.

• External gas heated mainly by feedback.

These different types of the hot CGM could in principle contribute differently in different types of galaxies, and show different morphological, physical, and chemical properties (e.g., Fig. 2; Li & Wang 2013b; Li et al. 2014, 2017a).

If the mass of the dark matter halo is high enough (typically for super-L* galaxies with $M_{\rm halo} \gtrsim 3 \times 10^{11}$ $M_\odot$; e.g., Kereš et al. 2005; Bregman et al. 2018), externally accreted gas could be gravitationally heated (either by weak shock or gravitational compression) to the virial temperature of the galaxy, which is in the X-ray emitting range. At this temperature, the cooling timescale is long enough so the gas cannot cool efficiently before being accreted around the galactic disk (e.g., Kereš et al. 2005; White & Frenk 1991). This gravitationally heated X-ray emitting external gas is a main prediction of the ΛCDM cosmology (e.g., Toft et al. 2002; Crain et al. 2010), and has been searched for around some massive isolated quiescent galaxies (e.g., Benson et al. 2000). Based on latest observations in recent years, the extended large-scale X-ray emissions are often not as strong as those produced by the internal gas (see below), and the hot CGM often contains just a small fraction of the expected baryon budget of the galaxy (e.g., Li et al. 2006, 2007; Rasmussen et al. 2009; Anderson & Bregman 2011; Dai et al. 2012; Bogdán et al. 2013, 2015; Li et al. 2014, 2016c, 2017a, 2018; Hodges-Kluck et al. 2018; see however estimate of the baryon budget of an extended hot CGM based on extrapolation of the density profile in Bregman et al. 2018, 2022).

Internal gas mainly from stellar mass loss could also be heated gravitationally to X-ray emitting temperatures during the orbital motion of the stars in massive enough galaxies (e.g., Forman et al. 1985). This component is distinguishable from the gravitationally heated external gas for its higher metallicity and more concentrated spatial distribu-

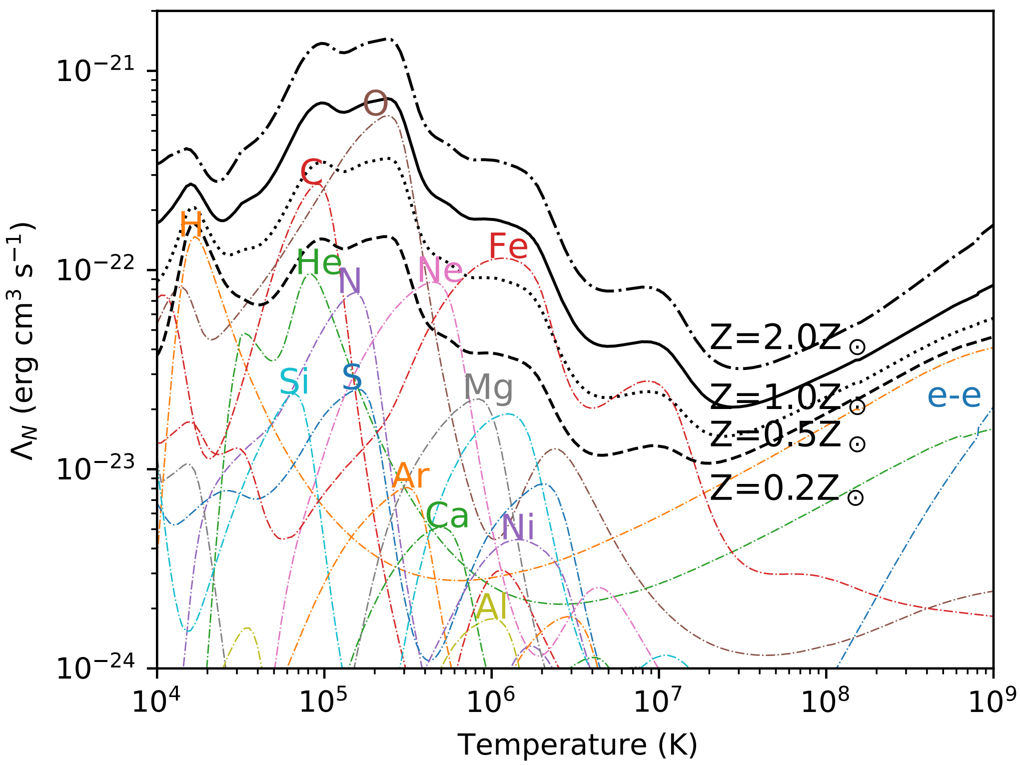

Figure 1. Radiative cooling curve of the thermal plasma under CIE based on the AtomDB data base (http://www.atomdb.org). The vertical axis is the normalized radiative cooling rate of the plasma defined as: $\Lambda_N \equiv \frac{U}{\tau_{\rm cool} n_{\rm e} n_{\rm t}}$ (in unit of erg cm^3 s^{-1}), where U is the internal energy of the gas [$U = \frac{3}{2}(n_{\rm e} + n_{\rm t})kT$], $\tau_{\rm cool}$ is the radiative cooling timescale, while $n_{\rm t}$ and $n_{\rm e}$ are the total ion and electron number densities, respectively. The horizontal axis is the temperature of the plasma. Different colored dash-dotted curves are the contribution by different elements (we only consider 14 elements with the strongest emissions) assuming an abundance of $Z = 1.0\ Z_\odot$ (adopting the abundance of different elements from Anders & Grevesse 1989), with "e-e" denote the electron-electron bremsstrahlung emission. The thick black curves are the sum of all these components under different abundances (the dashed, dotted, solid, and dash-dotted curves correspond to $Z = 0.2, 0.5, 1.0, 2.0\ Z_\odot$, respectively).

tion around the galaxy (e.g., Humphrey & Buote 2006; Li et al. 2009; Li 2015). Since galaxies massive enough to heat their stellar ejecta to X-ray emitting temperatures are often the cD galaxies of massive clusters, this hot CGM component is often mixed with the ICM (e.g., Forman & Jones 1982; Jones & Forman 1984; Fukazawa et al. 2006; Sun et al. 2009). The gravitationally heated internal gas is also distinguishable from the internal gas mainly heated by galactic feedback, because they have clearly different scaling relations between the X-ray luminosity and the galaxy mass tracers (galaxy mass, optical/IR luminosity, halo mass, rotation velocity, velocity dispersion, etc.). The gravitationally heated component (often in massive elliptical galaxies) shows a much steeper scaling relation than the feedback heated component (often in disk star forming galaxies), but the scaling relation is less steep than more massive systems such as galaxy groups and clusters (e.g., Ponman et al.

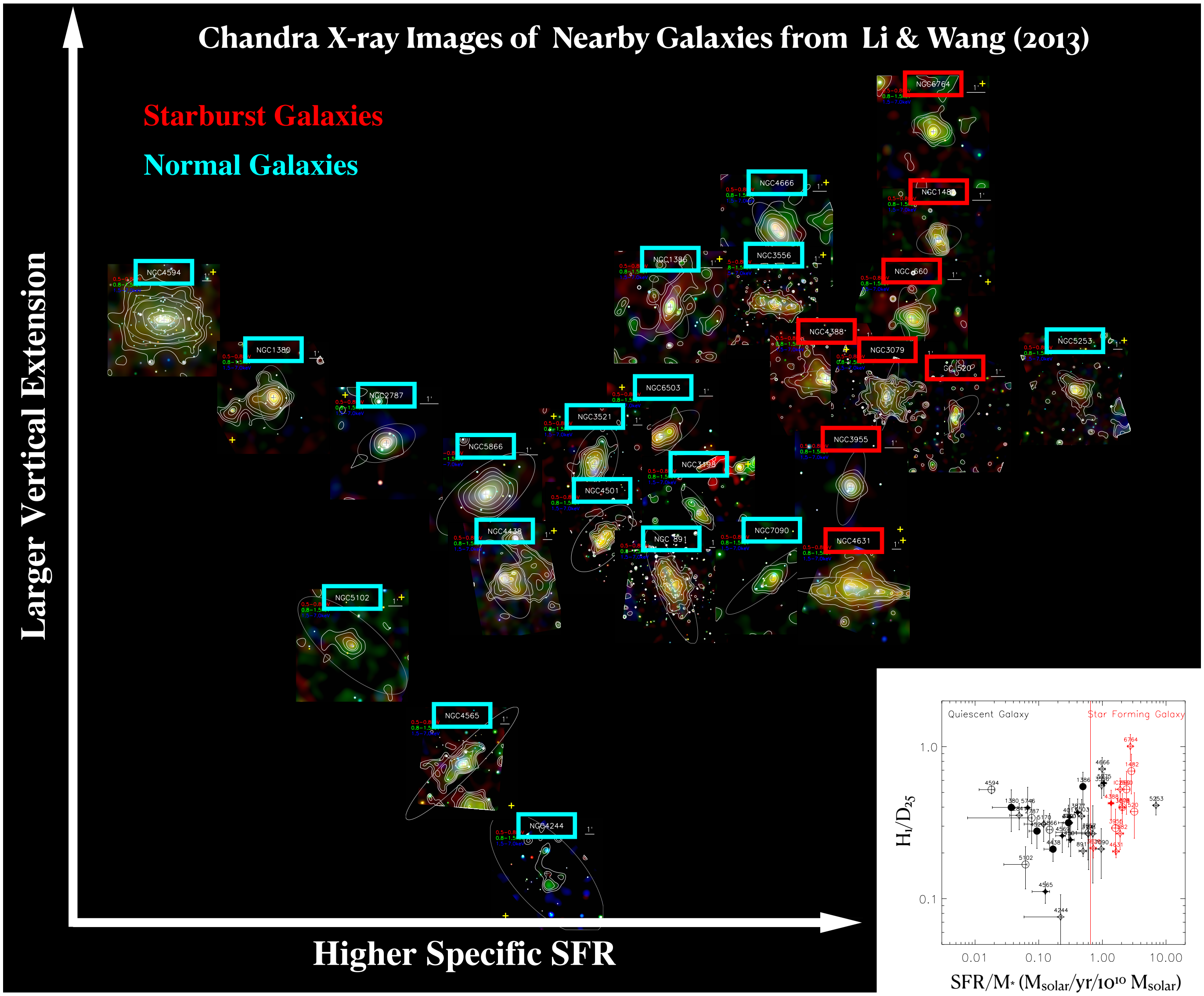

Figure 2. Soft X-ray morphology of galaxies with different mass and SF properties. Images are adapted from Li & Wang (2013a)'s *Chandra* sample of nearby edge-on disk galaxies. The inserted panel on the lower right corner is the plot of H_1/D_{25} against SFR/M_*, where H_1 is the vertical extension of the diffuse soft X-ray emission measured at a fixed intensity of 5 counts s^{-1} arcmin^{-2}, D_{25} is the blue diameter at the 25$^{\rm th}$ mag arcsec^{-2} isophote, and M_* is the stellar mass of the galaxy. The galaxies are clearly distributed in at least two branches separated by $SFR/M_* \sim$ 0.65 $M_\odot$ yr^{-1}/(10^{10} $M_\odot$). Starburst galaxies with a higher SFR/M_* show a positive dependence of H_1/D_{25} on SFR/M_*, indicating that galaxies with more active SF tends to have more vertically extended hot CGM. On the other hand, quiescent galaxies with lower SFR/M_* show a negative dependence of H_1/D_{25} on SFR/M_*, indicating that more massive galaxies tend to have a less vertically extended hot CGM. We plot the soft X-ray images (with contours) of Li & Wang (2013a)'s sample in the background. The locations of the galaxies are roughly consistent with those plotted in the inserted panel. Starburst galaxies are marked with a red box, while normal non-starburst galaxies are marked with a cyan box.

1996; Boroson et al. 2011; Kim & Fabbiano 2015; Li & Wang 2013a,b; Li et al. 2017a; Babyk et al. 2018).

Galaxies often have energetic outflows, which could be produced by various types of galactic feedback, such as AGN, active star formation, or even Type Ia supernovae (SNe) in relatively quiescent environments (e.g., Strickland & Stevens 2000; Tang et al. 2009). These outflows, when interacting with the surrounding medium or the entrained gas clouds, could produce strong X-ray emissions (e.g., Strickland et al. 2002). Here we emphasize that the feedback is often believed to dominate the X-ray emission, but may not dominate the total amount of the heated gas (e.g., Crain et al. 2013). This is because the feedback heated internal gas often has higher density and metallicity, so disproportionally strong in X-ray emission than the low density external gas (X-ray emissivity $\propto n_{\rm e}^2 Z$, where $n_{\rm e}$ and Z are the electron number density and metallicity, respectively). The major types of galactic feedback include the energy injection by AGN, or the energy and metal-enriched matter injection by old (Type Ia SNe) and young stellar populations [core collapsed (CC) SNe or massive stellar wind]. An accurate measurement of the metallicity pattern (often expressed in the Fe/O abundance ratio) will be the most direct way to study the origin of the hot CGM from feedback (e.g., Li 2015; Mao et al. 2021). However, in most existing X-ray observations of local galaxies, we do not have sufficient number of photons nor high enough energy resolution to accurately measure the metallicity (e.g., Hodges-Kluck et al. 2018). In most of the cases, we identify the origin of the hot CGM as produced by feedback in two ways: (1) individual extended X-ray features directly connected to either the AGN (e.g., Machacek et al. 2004; Li et al. 2019) or disk star formation regions (e.g., Strickland et al. 2004a; Tüllmann et al. 2006a; Li et al. 2008; Li & Wang 2013a; Hodges-Kluck et al. 2020); (2) statistical scaling relations connecting the hot CGM properties to various tracers of stellar feedback [e.g., star formation rate (SFR), SNe energy injection rate, Hα, IR or radio luminosities, etc.; Strickland et al. 2004b; Tüllmann et al. 2006b; Li & Wang 2013b; Wang et al. 2016; Jiang et al. 2019].

In principle, feedback could also heat the external gas. There exist large-scale hot CGM features around some galaxies, but the heating mechanism of the hot gas is often not clearly determined (e.g., Stevens et al. 2003; Li et al. 2008; Hodges-Kluck et al. 2020). The efficiency in heating the external gas by feedback largely depends on the properties (density and temperature) of the gas. If the surrounding gas is too hot, the sound speed is high so the shocks produced by feedback is likely weak with low Mach numbers. In this case, the heating is often less efficient and the feedback energy could be transported to larger scales without losing too much energy via cooling (e.g., Tang et al. 2009). On the other hand, when there exist large scale cool gas clouds surrounding the galaxy, we can sometimes see strong ionized gas features up to $\sim 10^2$ kpc scale, which could be heated by feedback (e.g., Rupke et al. 2019; Hodges-Kluck et al. 2020).

1.2. *Existing Key Results on the Hot CGM*

Based on a few decades of X-ray observations of nearby galaxies with many telescopes, such as the *Einstein*, *ROSAT*, *ASCA*, *Chandra*, *XMM-Newton*, *Suzaku*, and *eROSITA*, etc., we now have a few key results on the hot CGM:

• *Decomposition of different X-ray emission components.* The X-ray emission in and around local galaxies after subtracting various foreground or background components could in general be decomposed into a few components: AGN, individually detected stellar sources, unresolved stellar sources, and hot gas (e.g., Li et al. 2007; Revnivtsev et al. 2007a,b, 2008; Li 2015; Li et al. 2016c, 2017a). In many cases we can see an excess in soft X-ray emission after removing the stellar and AGN components. This soft excess is often believed to be produced by the hot gas. Extended diffuse hard X-ray emission is detected in a few cases, which could sometimes be explained as the non-thermal synchrotron emission from CR leptons (e.g., Li et al. 2019). But such a component is not commonly detected in most of the galaxies.

• *Spatial distribution of the hot CGM.* Diffuse soft X-ray emission extending beyond the stellar content of galaxies is also ubiquitous in different types of galaxies (e.g., Fig. 2; Forman et al. 1985; Li & Wang 2013a; Kim et al. 2019). The morphology of the diffuse X-ray emission shows some coherent structures as the extended features in other wavelengths, but the fine structures are often clearly different (e.g., Strickland et al. 2004a; Tüllmann et al. 2006a). This diffuse soft X-ray emission component, beyond but often close to the galaxy (e.g., at $r < 10 - 20$ kpc), is often expected to be produced during the disk-halo interaction, when the real hot tenuous gas mixes and physically interacts with the cool gas (e.g., Strickland et al. 2002; Li & Wang 2013b). This component, due to its high density, often dominates the diffuse soft X-ray emission around galaxies. On the other hand, there also exists an extended hot CGM component, which is mostly comprised of the real hot gas close to the virial temperature of the dark matter halo, and distributes within the entire or at least a significant fraction of the galaxy's dark matter halo (e.g., Anderson & Bregman 2011; Anderson et al. 2013; Dai et al. 2012; Bogdán et al. 2013; Li et al. 2017a, 2018; Bregman et al. 2018, 2022).

• *Physical and chemical properties of the hot CGM.* Because of the low spectral resolution and counting statistic of most of the X-ray imaging spectroscopy observations, the physical and chemical properties of the hot CGM is often poorly constrained (e.g., Strickland et al. 2004a; Tüllmann et al. 2006a; Li & Wang 2013a). The diffuse X-ray spectrum is often fitted with a 1-T or 2-T model with a fixed metallicity pattern (i.e., the abundance ratio between different elements is fixed; e.g., Li & Wang 2013a), although in some very limited cases some more detailed analysis can be conducted (e.g., Humphrey & Buote 2006; Li 2015; Anderson et al. 2016; Hodges-Kluck et al. 2018; Lopez et al. 2020). The obtained temperature of the hot gas is often $kT \lesssim 1$ keV, while the metallicity is typically subsolar or moderately supersolar, especially in late-type galaxies rich in cool gas. This indicates that the detected extended X-ray emission around galaxies is mostly produced by the mixed gas from the surrounding cool CGM and the metal-enriched hot gas outflow. In most of the cases, the hot, tenuous, and metal-enriched SNe ejecta is not unambiguously detected in X-ray, although there are claims of the detection of such ejecta in some special cases (e.g., Strickland & Heckman 2009).

• *Statistics of the hot CGM.* Different types of galaxies follow different scaling relations between the hot CGM properties (X-ray luminosity, vertical or radial extension, hot gas temperature, entropy, etc.) and other galaxy properties (stellar mass, gravitational or dark matter halo mass, SFR, etc.; e.g., Forman et al. 1985; O'Sullivan et al. 2003; Strickland et al. 2004b; Boroson et al. 2011; Li & Wang 2013b; Wang et al. 2016; Jiang et al. 2019). The hot CGM is distinguishable from the IGrM, ICM, or IGM for their typically lower temperature, lower luminosity per unit stellar mass, and smaller extension (e.g., Ponman et al. 1996; Sun et al. 2009; Kim & Fabbiano 2015; Li et al. 2017a; Babyk et al. 2018).

1.3. *Unresolved Problems*

In addition to the relatively firm conclusions as summarized above, there are also some key sciences related to the hot CGM which cannot be well addressed based on existing observations:

• *Decomposition of different hot CGM components.* As introduced in §1.1, the hot CGM could be classified into four different types based on the major heating mechanism and the origin of the gas. The most direct way to decompose these different components would be a spatially resolved spectroscopy analysis with a high energy resolution, in order to characterize the spatial variation of the physical, chemical, and dynamical properties of the hot CGM (e.g., Anderson et al. 2016; Hodges-Kluck et al. 2018; Lopez et al. 2020). However, in most of the existing X-ray observations, this is impossible due to the limited number of X-ray photons and the low energy resolution of the CCD spectra (e.g., Strickland et al. 2004a; Tüllmann et al. 2006a; Li & Wang 2013a). The low energy resolution prevents us from decomposing different X-ray emitting components, as well as separating and measuring individual emission lines above the continuum in soft X-ray in order to directly constrain the metallicity (e.g., Liu et al. 2011, 2012; Zhang et al. 2014b; Lopez et al. 2020).

Another way to decompose different hot CGM components is to conduct statistical analysis of large galaxy samples. Existing X-ray surveys based on archival *Chandra*, *XMM-Newton*, or *Suzaku* data often focus on certain types of galaxies (starburst, normal spiral, or elliptical, etc.), and is often limited on the sample size (typically a few tens of galaxies; e.g., O'Sullivan et al. 2003; Strickland et al. 2004b; Tüllmann et al. 2006b; Li & Wang 2013b; Boroson et al. 2011; Kim & Fabbiano 2015). As different types of galaxies are expected to follow different X-ray scaling relations, the small sample size and the mixture of different types of galaxies often lead to large scatter in the scaling relation, which prevents a clear understanding of the origin of the hot CGM (e.g., Li et al. 2014).

Future X-ray observations, either with a higher energy resolution X-ray imaging spectrograph (e.g., the micro-calorimeter on board *XRISM*), or a moderately deep survey of a large number of different types of galaxies (e.g., *eROSITA*), are expected to help us to better understand the origin of the hot CGM around different types of galaxies.

• *Baryon budget of the hot and multi-phase CGM.* Around local galaxies, the observed amount of baryons in stars and multi-phase gases is often significantly lower than the expected cosmic baryon fraction (e.g., Bregman 2007; Bregman et al. 2022). A significant fraction of these "missing baryons" could be stored in the extended diffuse hot CGM. Limited by the systematical and statistical uncertainties of the sky background, especially the contamination from the hot halo of the MW, we cannot detect very low surface brightness X-ray emissions from the extended hot CGM. Based on existing X-ray observations, we can typically detect the hot CGM only to $\sim 10\% - 20\%$ of the virial radius of the dark matter halo of a massive quiescent galaxy (e.g., Dai et al. 2012; Bogdán et al. 2013, 2015; Anderson et al. 2016; Li et al. 2016c, 2017a). The radial range with firm detections of the X-ray signals could be expanded based on stacking X-ray images of well selected galaxy samples, but still limited by the sky background with considerable statistical uncertainties (e.g., Anderson et al. 2013; Li et al. 2018). The difficulties in detecting the extended hot CGM on large scales strongly increase the uncertainty in estimating the total baryon mass contained in the hot CGM (e.g., Bregman et al. 2018).

Some future X-ray telescopes, such as *HUBS* (§2), will be equipped with higher energy resolution imaging spectrometers. The higher energy resolution will be helpful to better constrain the gas metallicity, so reduce the uncertainties in estimating the gas density and total mass (since the directly measured X-ray emission measure $EM \propto n_e^2 Z$; e.g., Bogdán et al. 2013; Li et al. 2016c, 2017a). More importantly, the high energy resolution also allows us to separate the soft X-ray emission lines of the hot CGM of an external galaxy from the same lines in the MW halo. This will enable narrow-band imaging with significantly reduced sky background, allowing us to probe the hot gas distribution to much larger radii (e.g., Li 2020). Combined with the large effective area and sometimes also large FOV of some future X-ray missions (see comparisons in §2 and Fig. 3a), we could better characterize the spatial distribution of the hot CGM, and separate it from the IGrM or ICM based on their distinct temperature profiles (e.g., Sun et al. 2009; Anderson et al. 2016). These improvements from future X-ray telescopes will help us to better constrain the amount of hot baryons stored in the extended hot CGM.

• *Galactic feedback mechanisms.* In most of the $L^\star$ or sub-$L^\star$ galaxies, the diffuse X-ray emission around the galaxies could be attributed to the internal gas heated by young and/or old stellar populations, in the form of galactic outflows produced by SNe or massive stellar wind (e.g., Strickland & Stevens 2000; Tang et al. 2009). However, only a small fraction (typically $\sim 1\%$) of the expected SNe feedback energy has been detected in X-ray emissions from the hot CGM (e.g., Li & Wang 2013b). This fraction is almost a constant over a few orders of magnitude, which is unexpected if both the thermalization efficiency of the feedback energy and the mass loading factor of cool gas depend on the SFR (e.g., Zhang et al. 2014a). This "missing feedback" problem could be interpreted if the SNe energy has been deposited into other CGM phases (e.g., Faerman et al. 2020), or simply transported outward as a radiative inefficient subsonic flow (e.g., Tang et al. 2009; Wang 2010). A complete multi-wavelength census of the energy budget in different CGM phases is still missing, which requires high-quality multi-wavelength data (e.g., Li et al. 2016a).

On the X-ray side, future high sensitivity, high energy resolution observations of the hot CGM around local galaxies will help us to better constrain the thermal and chemical structure, as well as the spatial distribution of the hot CGM (e.g., Hodges-Kluck et al. 2018; Lopez et al. 2020). This will help us to measure the gas density and the sound speed in the hot CGM, thus examine if the SNe driven outflow is radiatively efficient or not (e.g., Li et al. 2009). We may also be able to characterize the broadening of individual emission lines in some extreme cases, and estimate the energy stored in the form of turbulence (e.g., Hitomi Collaboration et al. 2016). Furthermore, high-quality multi-wavelength observations available now or in the future will also help us to investigate the role of other CGM phases (e.g., CR and magnetic field; Irwin et al. 2012a,b; Ruszkowski et al. 2017; Krause et al. 2020) or other forms of energy injection (e.g., turbulence in cooler gas phases; Zhuravleva et al. 2014; Boettcher et al. 2016; Li et al. 2020) in the dynamics of the hot CGM.

• *Gas cycling between the ISM, CGM, and IGM.* The hot CGM is a key point in the chain of gas cycling in and out of galaxies. In the close vicinity of the galaxies, the ratio between the radiative cooling timescale and dynamical timescale of the hot CGM could be small enough, so the gas could cool and precipitate onto the galaxies as fresh fuels in the ISM to continue star formation (e.g., Voit & Donahue 2015; Voit et al. 2015; Li et al. 2017a). On the other hand, stellar feedback could also deposit energy and metal-enriched materials into the CGM or even the larger scale IGM. In this gas cycling processes, many physical processes may affect the balance between the amount of gas stored in the hot CGM/IGM and the cool star forming ISM, such as the enhanced cooling caused by the cool-hot gas interaction (thermal conduction, evaporation, turbulent mixing, or even CX; e.g., **ref?**). Systematic comparisons between the radiative cooling rate of the hot CGM, the amount of cold gas in the galaxies, and its SFR are limited by the availability of high quality multi-wavelength data in different types of galaxies. At least in most of the $L^\star$ or sub-$L^\star$ disk star forming galaxies, the radiative cooling of the hot CGM seems insufficient to compensate the gas consumed in star formation, indicating additional star formation fuels (accretion of cold gas, merger, etc.) should be present (e.g., Li & Wang 2013b; Li et al. 2017a).

With future X-ray telescopes, we can better characterize the radial (in elliptical or face-on spiral galaxies) or vertical (in edge-on spiral galaxies) distribution of the hot gas radiative cooling timescale (e.g., Li et al. 2017a). This is critical to be compared to theoretical models to understand the thermodynamics of the hot CGM, which always shows significant spatial variations. The high energy resolution spectra will also help us to investigate some other physical processes involved in the X-ray emissions other than thermal and ionization equilibrium plasma emissions, such as the CX (e.g., Liu et al. 2011, 2012; Wang & Liu 2012; Zhang et al. 2014b). Some of these processes may even dominate the emission in some certain bands, so strongly biases the measurement of the hot gas cooling rate. Furthermore, high quality multi-wavelength data available in the future will also help us to investigate the role of other CGM phases in the gas cycling (e.g., Tumlinson et al. 2011, 2017; Werk et al. 2014).

2. A BRIEF INTRODUCTION OF HUBS

The Hot Universe Baryon Surveyor (*HUBS*; Cui et al. 2020) is a space X-ray telescope with the primary scientific objective focusing on the census of baryons in the warm-hot CGM/IGM and thus to directly address the issue of "missing baryons" in the local universe. *HUBS* could also be used to study a variety of scientific topics, including but not limited to the Galactic objects, MW and local galaxies, AGN, and large-scale structures, etc.

2.1. *Compare HUBS to other X-ray missions*

In order to achieve its scientific goals, *HUBS* combines a large field of view (FoV; 60×60 array with a FoV of $\Omega_{\rm FoV} \sim 1\ {\rm deg}^2$), high energy resolution ($\Delta E = 2$ eV, or $R \equiv E/\Delta E \sim 500$ @ $E \sim 1$ keV), and high sensitivity (effective area $A_{\rm eff} \gtrsim 500\ {\rm cm}^{-2}$ @ $E \sim 1$ keV) in the soft X-ray band ($0.1 - 2$ keV), which are optimized to study the diffuse hot plasma on various physical scales. The high energy resolution will be achieved by employing a superconducting transition-edge sensor (TES)-based micro-calorimeter (Cui et al. 2020). The requirement on the angular resolution ($\sim 1'$), however, is not quite high for the study of extended sources. In Fig. 3a, we compare the Figure-of-Merit in the detection of emission lines from extended sources ($FoM_{\rm em}$) of the key instrument on board a few X-ray telescopes either in operation or under development (also see Li 2020). The $FoM_{\rm em}$ is defined as:

$$FoM_{\rm em} = RA_{\rm eff}\Omega_{\rm FoV}. \quad (1)$$

HUBS is obviously outstanding in the study of emission lines from extended sources for its high energy resolution, large effective area and FoV.

For absorption line studies of X-ray bright background sources, the Figure-of-Merit ($FoM_{\rm ab}$) is not affected by the FoV:

$$FoM_{\rm ab} = RA_{\rm eff}. \quad (2)$$

In this case, *HUBS* is less outstanding but still excellent. Furthermore, it also has a 12×12 central sub-array with a smaller pixel size ($15''$) and higher energy resolution ($\Delta E = 0.6$ eV), which is optimized for absorption line studies (Fig. 3b). In many cases, a combination of the emission line studies with the normal array and the absorption line studies with the central sub-array will be very efficient to jointly constrain the hot gas properties (see examples of science cases in §3).

2.2. *HUBS observation strategy in the study of the hot CGM*

Based on the technical design (large FOV and low angular resolution), in most of its studies of the hot CGM, *HUBS* is optimized to take observations in two modes: either deep exposure of some objects with moderate angular sizes, or a shallow or moderately deep survey of a large sky area (including a possible all sky survey; §3.1). For example, in the former case, a single-pointing *HUBS* observation could cover a significant fraction of the dark matter halo of a local galaxy (the *HUBS* FOV covers the entire dark matter halo of a $L^\star$ galaxy at $d \sim 50$ Mpc; e.g., Li 2020, §3.2.4). On the other hand, *HUBS* is also optimized to study some more nearby objects in our local neighbourhood with an angular size of tens or hundreds of deg^2 (e.g., $\sim 200 - 300$ HUBS observations are needed to cover the entire M31-M33 group; §3.2). We herein summarize a few key differences between these two modes:

• *Survey or observation strategy.* The angular size of the hot CGM around a $L^\star$ galaxy (expected to be the most abundant in baryons; e.g., Bell et al. 2003; Bregman et al. 2022) at a distance of $d > 10$ Mpc is relatively small. For example, the virial radius of NGC 891 ($M_* \approx 4 \times 10^{10}\ {\rm M}_\odot$, rotation velocity $v_{\rm rot} \approx 212\ {\rm km\ s^{-1}}$, $d \approx 9.1$ Mpc; Li et al.

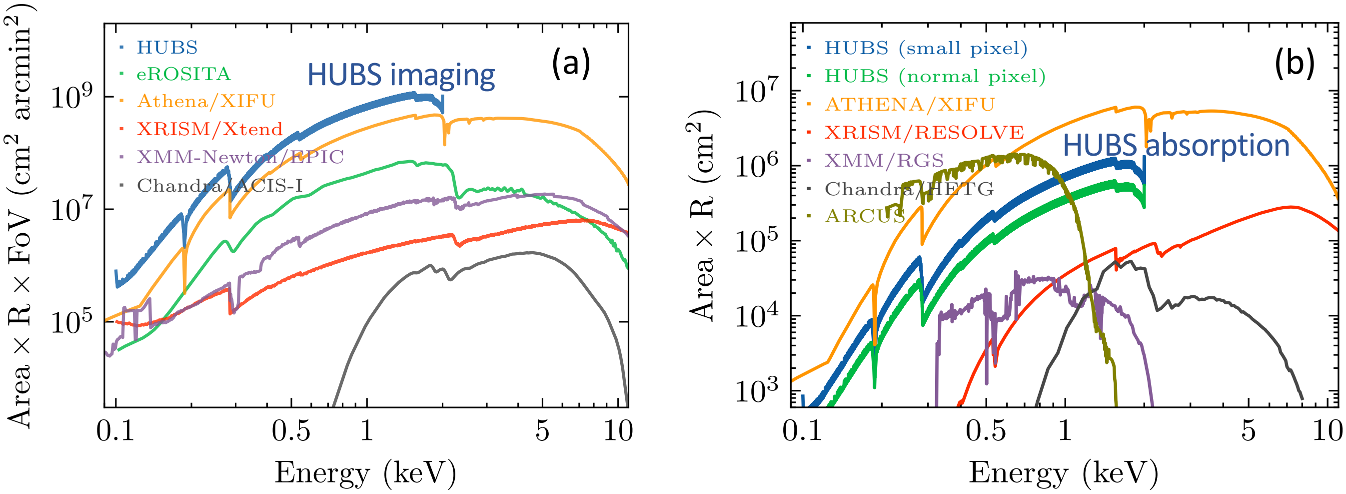

Figure 3. Comparison of the FoM of a few X-ray missions in the detection of emission lines from an extended source (a; $FoM_{\rm em}$) and absorption lines from a point-like source (b; $FoM_{\rm ab}$). The normal pixels' response of HUBS are used in (a), while center small pixels' and normal pixels' are both used in (b). For grating instruments (XMM/RGS, Chandra/HETG and ARCUS), all available grating orders are combined.

2016a) is $r_{200} \sim 1.5°$ (e.g., Li 2020). For galaxies with similar mass at larger distances, *HUBS* could cover $r \gtrsim 30\% r_{200}$ in a single observation centered at the galaxy. This is typically sufficient to characterize the spatial distribution of the hot CGM, as hot gas on larger scales is not commonly detected in existing X-ray observations of a single quiescent galaxy (e.g., Bogdán et al. 2015; Li et al. 2017a).

On the other hand, some nearby objects in the MW and LG often have a much larger angular size which cannot be easily covered by *HUBS* in just a few observations. For example, the virial radius of M31 is $r_{200} \sim 15°$ (§3.2), and a single *HUBS* observation could only cover $r \lesssim 3\% r_{200}$. In these cases, mosaic is often needed and each observation could only be moderately deep. The advantages in the observations of these nearby objects are the relatively low point source detection limit and high angular resolution in physical size, so it is much easier to cleanly remove the point source contributions. A quantitative estimate of the point source contribution is critical in the study of faint hot gas emissions, especially in *HUBS* observations where the hard X-ray at $\gtrsim 2$ keV typically dominated by AGN and X-ray binaries is not covered (e.g., Revnivtsev et al. 2007a, 2008; Li & Wang 2013a; Huang et al. 2023a).

• *Combination with X-ray absorption line studies.* There are few X-ray bright point-like sources residing outside the MW which could be used as background sources for absorption line studies (sometimes we can also use X-ray sources inside the MW; e.g., Yao & Wang 2005; Luo et al. 2018). Most of these background sources are AGN (e.g., Rasmussen et al. 2003; Fang et al. 2006; Bregman & Lloyd-Davies 2007; Miller & Bregman 2013), while some are X-ray bright stellar sources residing in nearby galaxies (e.g., Wang et al. 2005; Cabot et al. 2013). Due to the low spatial density of these background sources, it is often difficult to find multiple sightlines of them projected behind a distant galaxy with small angular sizes. Therefore, the only object feasible for an intense absorption line study of the hot CGM is the MW, and possibly in some LG galaxies with large angular sizes [M31, large and small Magellanic Clouds (LMC and SMC), etc.]. The X-ray emission line strength is $\propto n_{\rm e}^2 V$, while the X-ray absorption line strength is $\propto n_{\rm e} l$, where V and l are the volume or the line of sight length of the X-ray emitting regions. Combining the emission and absorption line studies could thus provide us with a unique probe of the spatial structure of the X-ray emitting gas (e.g., characterized with the volume or linear filling factor f).

• *Combination with multi-wavelength data.* X-ray study of the hot CGM alone has a lot of systematic uncertainties, such as the metallicity-density degeneracy, the effect of complicated thermal structure of the plasma, the contributions of non-thermal emission and background components, the scattered photons from bright point-like sources, etc. (e.g., Li et al. 2016c, 2017a). A joint analysis with the multi-wavelength data is a key method to evaluate these uncertainties.

Most of the high-quality multi-wavelength data are available only in very nearby and well studied galaxies (including the MW itself). For example, we could often find sufficient number of UV bright background AGNs to sample the spatial distribution of lower temperature gases in the MW or some LG galaxies (e.g., Fox et al. 2014, 2015; Lehner et al. 2020; Qu et al. 2020). When combined with the X-ray absorption or emission line data (e.g., Miller & Bregman 2013, 2015), this could greatly help us to understand the thermal structure of the multi-phase CGM (e.g., Faerman et al. 2017, 2020; Qu & Bregman 2018). Thanks to the rotation measure (RM) measurements of the radio bright pulsars or other extragalactic sources, we also have a much better knowledge on the magnetic field of the MW halo than in other galaxies (e.g., Han et al. 1999, 2018; Beck 2012; Noutsos 2012; Sobey et al. 2019; Krause et al. 2020). This will help us to investigate the role of large scale magnetic field in the dynamics of the hot ionized gas flows (e.g., Irwin et al. 2012b; Li et al. 2022). Furthermore, there are also some other non-X-ray probes of the hot ISM/CGM/IGrM which are only widely adopted in the study of the MW and LG. For example, the dispersion measure (DM) of fast radio bursts (FRBs) or radio pulsars is also a powerful tool to study the hot gas, but in most of the cases only for the hot ISM/CGM of the MW could we find a sufficient number of these radio bright sources to sample the spatial distribution of the DM (e.g., Prochaska & Zheng 2019; Prochaska et al. 2019; Han et al. 2021).

Due to their relatively small angular sizes, high-quality multi-wavelength imaging data tracing various gas phases in the CGM are often available for external galaxies at moderate distances (typically a few to a few tenth of Mpc; e.g., Rossa & Dettmar 2003; Walter et al. 2008; Veilleux et al. 2009; Vargas et al. 2019; Zheng et al. 2022). In particular, the best SZ data, which is another key probe of the hot gas, is often available in moderately distant galaxies with moderate angular sizes (e.g., Bregman et al. 2022). This is because the SZ signal is strongly affected by the large scale dust features in the MW foreground, so easier to remove in a small uniform field. As the observed X-ray emission measure $EM_{\rm X} \propto Zn_{\rm e}^2$ (Z is the metallicity, $n_{\rm e}$ is the electron number density), the poorly constrained Z in low resolution X-ray spectra becomes one of the most important systematic uncertainties in the measurement of the density and mass of the hot CGM (e.g., Li et al. 2017a). On the other hand, the SZ signal $y \propto N_{\rm e}\langle T\rangle$, where $N_{\rm e}$ is the electron column density and T is the temperature of the hot gas. In general, $EM_{\rm X}$ is insensitive to T while y is insensitive to Z. Therefore, a joint analysis of the X-ray and SZ data could greatly help us to measure the hot gas density profile and the extended hot CGM mass, without biases caused by the assumed metallicity and temperature profiles.

3. HUBS SCIENCE CASES ON THE GALACTIC ECOSYSTEMS

In the following subsections, we describe a few specific HUBS science cases related to the galactic ecosystems. Additional scientific ideas from the community are certainly welcome.

3.1. *A shallow all sky survey and the MW halo*

Do we need a shallow all sky survey, a moderate covering fraction (e.g., $\sim 20\%$) mapping of the sky, or simply discard the idea of an all sky survey? Please put your ideas here. See suggestions by different people in the commented text.

3.1.1. *The Physical and Chemical Properties of the MW Hot Gas — Contributed by Z. Qu and S. Zhang*

The Milky Way (MW) provides a unique opportunity to study its CGM in great detail as the most prominent galaxy covering the entire sky (Bregman 2007; Putman et al. 2012). The hot gas surrounding the MW disk encodes the feedback by gathering the materials, energy, and metals ejected from the disk, which provide unique insights into the MW growth (see the recent reviews Tumlinson et al. 2017; Donahue & Voit 2022). The initial hint of the MW hot gas was discovered by RASS, shown as the anti-correlation between the soft X-ray emission at 1/4 keV and the neutral hydrogen (e.g. Snowden et al. 1995). After ROSAT, high spectral resolution spectra obtained by Diffuse X-Ray Spectrometer (DXS) revealed that the soft X-ray emission was dominated by thermal emission of hot gas ($k_{\rm B}T \approx 0.1 - 0.2$ keV; McCammon et al. 2002). The understanding of the MW hot gas has been improved significantly by extensive observations in the past two decades (e.g., Henley & Shelton 2012; Gupta et al. 2012; Miller & Bregman 2013; Hodges-Kluck et al. 2016; Kaaret et al. 2020; Ponti et al. 2023). However, there are still unresolved problems on the hot gas properties in the MW, including the density, temperature, metallicity distributions, and contamination, which is mainly due to the low spectral resolution of existing instruments.

First, the density distribution of the hot gas is the key to the long-term missing baryon problem, which suggests that the baryonic mass in the stars and interstellar medium cannot account for the expected baryon mass using the cosmic average baryonic fraction (e.g., McGaugh et al. 2010). The gap between the expected baryons and detected baryons is $\approx 1 - 2 \times 10^{11}$ $M_{\odot}$. To investigate this problem, the projected two-dimension emission should be decomposed into the three-dimensional density distribution, which requires a survey of the sky in different directions. The ROSAT mission found that the soft X-ray emission is anti-correlated with H I column density, suggesting the distant origin of the hot gas, which could be the hot CGM of the MW (Snowden et al. 1995). With deep observations of more recent instruments, recent studies aim to deproject the two-dimensional distribution into three-dimensional distribution (e.g., Gupta et al. 2012; Miller & Bregman 2013, 2015; Nakashima et al. 2018; Kaaret et al. 2020). In general, there are three major large-scale structures of the hot gas in the MW, the bubbles around the galactic center, the disk, and the halo. However, different studies yield different hot gas density distributions. Some studies suggest a spherical halo-dominated distribution (e.g., Miller & Bregman 2015), while others suggest hat the soft X-ray emission is dominated by the disk component (e.g., Nakashima et al. 2018; Kaaret et al. 2020). These difference distributions could lead to variations in the estimated hot gas mass.

Adopting the halo-dominated scenario, different radial profiles also lead to significantly different masses within the virial radius (i.e., $\approx$ 250 kpc). Assuming a uniform distribution, the mass can be as large as 2×10^{11} $M_{\odot}$ (i.e., Gupta et al. 2012), while a power-law density distribution with a slope of $\approx$ 1.5 leads to a mass of $3 - 4 \times 10^{10}$ $M_{\odot}$ (e.g., Miller & Bregman 2015; Li et al. 2017b). An assumption of hydrostatic equilibrium leads to a declining but flatter profile at large radii than the power-law model, which results in a mass of 1×10^{11} $M_{\odot}$ (e.g., Faerman et al. 2017, 2020). These differences are significant to consider whether the missing baryons are confined within the virial radius.

In addition, the temperature and metallicity also affect the mass estimation, and provide unique constraints on the feedback processes. In X-ray observations, the direct measurements are the emission or absorption from the highly ionized species (e.g., O VII, O VIII, and Ne IX), which need ionization fractions and element abundances to convert metals to hydrogen for the total mass. Previous studies normally assume single temperature collision ionization equilibrium (CIE) models (e.g., APEC or MEKAL in XSPEC) and constant metallicity of $0.3 - 1.0\ Z_{\odot}$. The temperature of the MW hot gas was found to be $\approx 0.1 - 0.2$ keV, which is consistent with the expectation of virialized gas (e.g., Henley & Shelton 2013; Kaaret et al. 2020). Recently, multiple temperature structures are revealed in the MW hot gas. A super-virial component with temperatures of $0.5 - 0.7$ keV has been characterized in both X-ray emission and absorption (e.g., Das et al. 2019a,b; Ponti et al. 2023), which may trace the energetic feedback from the galaxy disk. This super-virial phase is detected over the entire sky by *HaloSat*, and shows correlation with the "warm" phase at the virial temperature (Bluem et al. 2022). However, this super-virial component may be the foreground contamination due to the hot corona of M dwarfs (Wulf et al. 2019), leading to uncertainties in the temperature distribution of the hot gas.

The metallicity of the hot gas is poorly constrained in observations. For example, by combining the O VII emission and absorption, Bregman et al. (2018) estimated the metallicity of $\approx 0.5 - 1.0\ Z_{\odot}$. Using the eROSITA deep field, Ponti et al. (2023) reported a metallicity of $\approx 0.05 - 0.10\ Z_{\odot}$. Such a difference can be induced by the background decomposition in the X-ray spectral modeling, which affects the determination of the hot gas emission continuum.

Finally, because the hot gas emission covers the entire sky, there are various foreground and background contamination sources that cannot be removed directly. The most prominent foreground contamination at < 1 keV is the solar wind charge exchange (SWCX), which is the induced charge exchange between the ionized solar wind and the neutral gas in the solar system. The O VII SWCX line emission could vary ≈ 4 counts $s^{-1}\ cm^{-2}\ sr^{-1}$ (line unit; L.U.) from maximum to minimum over a solar cycle, while the average of the MW hot gas O VII emission is a constant about 4 L.U. (Qu et al. 2022). The SWCX emission also depends on the location as a result of the difference of solar wind properties between the solar equator and polar, together with the neutral gas distribution (Pan et al. in prep.). The unresolved stellar emission is another source of foreground contamination, which may contribute significantly to the emission at 0.7 keV (see details in Wulf et al. 2019). In the MW dark matter halo, the warm-hot corona of the Magellanic System may also contribute to the observed soft X-ray emission (Krishnarao et al. 2022). In addition, the nearest galaxy M31 may host a hot gas halo similar to the MW and a hot gas bridge connecting the MW and M31 (Qu et al. 2021). These contaminations lead to uncertainties in the modeling of the MW hot gas, which cannot be removed from existing low-spectral resolution data.

With the HUBS observations, the understanding of the MW hot gas can be significantly improved with the higher sensitivity and spectral resolution:

• *The decomposition of the SWCX from the MW hot gas emission.* The O VII Kα exhibits a triplet at 561, 568, and 574 eV (i.e., forbidden, intercombination, and resonant), which show different line ratios in different emission mechanisms. In Figure 4, we show the simulated HUBS observations of the MW hot gas with an emission measure of $10^{-3}\ cm^{-6}$ pc and a temperature of 0.2 keV, and two SWCX models at solar minimum and maximum, adopting the parameters described in (Huang et al. 2023b). The resonant line dominates the triplet in the thermal ionization model, while the forbidden line is stronger in the SWCX emission. The spectral resolution of HUBS is $1 - 2$ eV could resolve these lines, and decompose the SWCX and MW hot gas emission, providing a SWCX-clean measurement of the MW hot gas.

• *Better constraints on the temperature distribution.* Now, a two-temperature scenario is proposed to explain the observed emission enhancement at 0.8 keV, while numerical simulations suggest continuous temperature distributions (e.g., Vijayan &

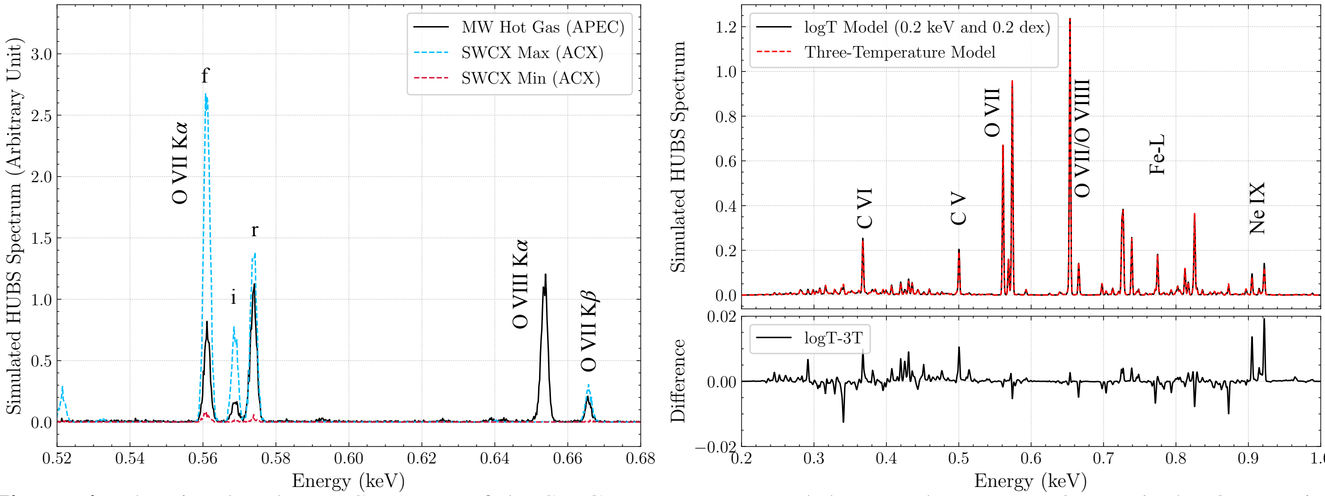

Figure 4. The simulated HUBS spectra of the SWCX component and the MW hot gas. *Left panel:* the O VII triplet generated by the SWCX exhibits a different resonant to forbidden line ratio. During the solar maximum, the SWCX can be stronger than the MW hot gas emission, while the SWCX is negligible during the solar minimum. *Right panel:* the comparison between the spectra of log-normal temperature and the three-temperature model. The difference between these two models is most significant at Ne IX triplet, which may be distinguished by HUBS observations.

Li 2022). The difference between these two scenarios is hardly distinguished by low resolution and low sensitivity. In Figure 4, we show the comparison between a log-normal distribution of the temperature and a three-temperature distribution. The log-normal distribution has a median temperature of 0.2 keV and a sigma of 0.2 dex, while the three-temperature model exhibits three components at 0.1, 0.2, and 0.48 keV. The maximum difference is 10% at the Ne IX triplet in this case, which is determined by the temperature distribution. Current low-resolution instruments cannot resolve such differences at all, while the HUBS may distinguish between the continuous temperature distribution and the separate temperature model by resolving weak lines.

• *The density distribution of highly ionized species.* The density distribution can be improved with the better corrected SWCX and the temperature distribution. First, the modeling of the hot gas density can be pushed beyond 50 kpc, which is the current limit enabled by existing instruments. Second, the disk and halo will be better decomposed, which will finally determine the total metal mass in the MW hot gas.

• *The constraints on the metallicity and non-solar abundance pattern.* New cosmic microwave background (CMB) experiments and improvement of Sunyaev-Zel'dovich (SZ) signal extraction will lead to better constraints on the SZ signal of the MW hot gas. The SZ signal extraction will not provide as high spatial resolution as the X-ray observations, but at the large scale, we will be able to constrain the metallicity and non-solar abundance pattern for multiple elements (e.g., C, O, Ne, and Fe), which will provide clues of the origin of the hot gas surrounding the MW.

■ Technical Justification

Most HUBS archives could be used to extract the MW hot gas emission as a byproduct because of its full sky coverage. Considering a lifetime of two years, there will be a sample of $\approx$ 5000 observations assuming the mean exposure time of 10 ks with an overhead of 2 ks, or $\approx$ 500 observations for 100 ks individual exposures. These observations could cover 0.5-1.0 % to 5-10% of the entire sky, considering repeated pointings. In addition, it is also possible to extend the HUBS mission with bonus observation times, which to enlarge the sky coverage. As a comparison, the 22-

year *XMM-Newton* archive covers $\approx 5\%$ of the sky with a median depth of 20 ks (Pan et al. in prep.). Therefore, because of the large FOV, we expect that the HUBS archive provides similar sky coverage as *XMM-Newton* within the first two years.

Using the XMM-Newton archive, the 5σ detection limit is $\approx 1.0-1.5$ LU for O VII triplet, O VIII Kα, and Fe-L emission (e.g., Henley & Shelton 2012; Pan et al. in prep.). With a high spectral resolution of $1-2$ eV, HUBS significantly reduces the background level, and enhances the detection sensitivity for diagnostic metal lines. According to Zhang et al. (2022a), 10 ks HUBS observation can have a 5σ detection limit of 0.032 LU for the O VII resonant line over the FOV of $1^\circ \times 1^\circ$, or about 1 LU for each $2' \times 2'$ pixel. The O VIII Kα line exhibits limiting intensities of 0.021 and 0.63 LU, respectively, while the detection limits of the Fe XVII 826 eV emission line are 0.024 and 0.72 LU. Using a spatial resolution equivalent to XMM FOV, the HUBS observation exhibits limiting 0.072, 0.047, and 0.054 LU for O VII, O VIII, and Fe XVII, respectively, which are one order of magnitude higher than existing *XMM-Newton* archive.

Such detection limits are sufficient to detect O VII, O VIII, and Fe-L emission in most sky, adopting the empirical model described in Qu et al. in prep. The 10 ks HUBS archive or follow-up survey could detect these diagnostic lines with a resolution of $1^\circ \times 1^\circ$, or O VII, it can be even detected for $2' \times 2'$ pixels. Combining the high sensitivity and spatial resolution, new HUBS observations could further improve the correlation of hot gas properties on small scales at $1-2^\circ$ or even arcmin. This correlation will provide strong constraints on the cosmic ray strength in the hot gas (e.g., Butsky et al. 2020).

3.1.2. *Mixing at the Disk-Halo Interface — Contributed by E. Hodges-Kluck*

Observations of edge-on galaxies (Strickland et al. 2004a; Tüllmann et al. 2006a; Li & Wang 2013a) and our own Milky Way (Kaaret et al. 2020) reveal that star-forming disk galaxies are surrounded by X-ray coronae with scale heights of several kpc (Tüllmann et al. 2006a; Li & Wang 2013a), whereas disk galaxies with little star formation lack such coronae. These coronae are clearly identified with ongoing star formation in the disk, and indeed in our Galaxy the emission is well described by a model where it sits above molecular gas in the disk (Kaaret et al. 2020). For many years, there was debate as to whether these coronae are "only" galactic fountains (Shapiro & Field 1976; Bregman 1980) or the inner parts of an extended, massive circumgalactic medium (CGM). Multiple lines of evidence now support the existence of hot CGM around $L*$ galaxies, such as Sunyaev-Zel'dovich (SZ) detections from nearby galaxies (Bregman et al. 2022), fast radio bursts (Prochaska & Zheng 2019), X-ray absorption through the Milky Way (Miller & Bregman 2013), and direct detection of X-ray emission around galaxies several times more massive than the Milky Way (Anderson & Bregman 2011; Bogdán et al. 2013; Li et al. 2017a). Hence, the answer must be "both": galactic coronae represent estuaries where outflows from the disk pour into the hot ocean of the CGM.

Studying these mixing regions is essential to understand the role of stellar feedback in the life of a Milky Way-like galaxy. The basic theory of galactic fountains (Bregman 1980; Mac Low et al. 1989) holds that overpressured superbubbles form around massive star clusters due to the action of fast stellar winds and supernovae (SNe) (Weaver et al. 1977; Silich et al. 2005) and expand until they break through the thin HI disk. The hot gas inside flows down the pressure gradient into the halo, where it cools and falls back. Hydrodynamic models (e.g., Hopkins et al. 2014; Kim & Ostriker 2018) show that a much greater mass of warm gas is entrained in these winds, and there is also cold gas and dust (Veilleux et al. 2020). Since angular momentum is conserved, when this material returns to the disk it tends to migrate to larger radii (Melioli et al. 2015).

Hence, fountains can disperse mass and metals over a wide area of the disk.

These processes occur in the absence of a hot atmosphere and in galaxies of any mass, but when one considers that the galactic fountain runs into hot CGM around a Milky Way-like galaxy, several additional processes can occur. First, the hot CGM can conductively heat cooler fountain gas to near the virial temperature. This heated gas is dense and has a short cooling time, so the fountains effectively stimulate cooling from the hot CGM (Marinacci et al. 2010; Armillotta et al. 2016) and bring "fresh" gas to the disk. The efficiency of stimulated cooling is unknown, but if the metallicity of the NGC 891 corona is indeed $Z/Z_{\odot} < 0.2$ (Hodges-Kluck et al. 2018) then much more hot CGM than hot ejecta returns to the disk. Secondly, these outflows can spin up the halo (Oppenheimer 2018) and produce lagging halos like the kind seen in HI (Sancisi et al. 2001; Fraternali et al. 2002; Oosterloo et al. 2007; Heald et al. 2011b). This, in turn, regulates accretion onto the disk, with different accretion rates expected from high angular momentum, smooth inflows than from precipitation of cooled, low angular momentum gas onto the disk. Thirdly, the amount of fountain gas that gets mixed into the CGM and migrates to large radii determines how metals escape galaxies. If the CGM provides an effective "ceiling" to the fountain flow, metals can only escape galaxies in major AGN our starburst outflows or at earlier cosmic times before a virialized CGM formed. Since the CGM is suffused with dust (Ménard et al. 2010) and galaxies are missing most of their metals (Peeples et al. 2014), it is important to know how much outflows from individual star clusters contribute to the CGM.

Although studying the interaction of outflows and the hot CGM at the disk-halo interface is a multiwavelength endeavor, X-ray spectroscopy is the major missing piece. Some key missing quantities include the mass, metallicity, energy content, and velocity of the hot gas flowing into the halo, the point at which mixing with the ambient CGM begins, and the mass-loading factor of the outflows relative to what returns to the disk.

Both high spatial resolution and high spectral resolution are needed to measure these quantities. For example, a vertical resolution better than about 500 pc is needed to measure the metallicity profile from the disk into the halo. To measure the metal *flux* we also need to know the velocity, which requires resolving individual strong emission lines, such as O VIII (654 eV). Measuring the mass requires an accurate knowledge of the emission measure distribution as a function of temperature, which also requires resolving individual strong lines. Based on the expected temperatures and velocities, and existing low-resolution X-ray spectroscopy, we can estimate requirements: $\Delta E < 5$ eV is needed to separate strong line complexes enough to measure the temperature distribution (based on X-ray grating spectra of stellar coronae), $\Delta E < 3$ eV is needed to accurately model charge exchange lines, which may contribute significantly (Zhang et al. 2022b), and $\Delta E < 2$ eV is needed to measure velocities in the $v < 500$ km s^{-1} regime we expect (with $\Delta E < 1$ eV needed for lower energy lines like O VIII). HUBS meets these requirements.

At $d = 10$ Mpc, $1''$ corresponds to about 100 pc, so Chandra-like angular resolution is needed to measure vertical profiles even for relatively nearby galaxies. However, the low energy resolution ($\Delta E > 50$ eV) of the Chandra imaging spectrometers has proven a limiting factor in characterizing galactic coronae. The regions of interest are too faint and crowed for grating spectroscopy, either with Chandra or XMM-Newton. Hence, the best way to make progress is to look within our own Galaxy, where superbubbles and their chimneys have a large angular extent.

Focusing on the Milky Way suggests a two-pronged HUBS program to make the required measurements. First, HUBS will characterize the material within well characterized Galactic superbubbles and/or chimneys. The best and brightest candidates are the Orion-Eridanus superbubble (Heiles et al. 1999) and the Carina Nebula (Seward et al. 1979), although it would also be worth observing RCW 38 (Wolk et al. 2002), M17 (Townsley et al. 2003), NGC 6334 (Ezoe et al. 2006), or other Galactic H II regions. The Orion-Eridanus bubble covers at least 500 deg^2, while Carina is much smaller at less than 4 deg^2. Other candidates could fit in 1-2 HUBS fields.

Despite its angular size, Orion-Eridanus is an excellent target because there is evidence that it already has blown out into the halo (Heiles et al. 1999) and that its gas temperature is similar to that in the broader halo (Fuller et al. 2023). HUBS can therefore map the gas properties from the generative Orion star cluster to the breakout (and possibly beyond). It is unnecessary to tile the entire nebula, as sampling different regions is sufficient. The combination of inner (0.6 eV) and main (2 eV) arrays will be able to accurately map the average temperature distribution, metal abundance ratios, and even mass flux towards the breakout.

The average surface brightness of the Orion-Eridanus region (0.5-2 keV) is a few $\times 10^{-11}$ erg s^{-1} cm^{-2} deg^{-2}. Carina is 5-10 times brighter. Assuming an average luminosity-weighted temperature of $kT \sim 0.2$ keV and solar metallicity, HUBS would detect at least 4 O VII or O VIII photons per 1 arcmin^2 in 1 ks. $S/N = 10$ in these key lines could then be achieved at the HUBS resolution limit in 25 ks per pointing. This suggests that a sample of $\sim$50 deg^2 from Orion-Eridanus could be mapped in 1 Ms, and Carina mapped in 100 ks. A similar exposure of about 100 ks is sufficient for most other Galactic bubbles, so the total program could be smaller than 2 Ms.

The second prong, which could also be achieved by an all-sky survey, involves observing the CGM directly above known massive star clusters old enough to have experienced multiple supernovae and comparing it to the broader average Milky Way CGM seen at high latitudes. There are several options for a smaller, targeted program that would ultimately be decided by observability and the nature of structures such as the North Polar Spur, which is likely the edge of the Fermi bubbles but could be (in part) a closer supernova remnant that fills much of the sky. In this case, a comparison of the halo gas between the Galactic anti-center and toward OB associations may be the optimal strategy. Regardless, the goal would be to measure the vertical temperature and chemical abundance ratio profiles and compare them to directions without massive clusters and to the interiors of superbubbles. Based on HaloSat surface brightnesses (Kaaret et al. 2020; Bluem et al. 2022), $\sim$20 deg^2 maps of about 25 ks each (a total of 500 ks per region) would be sufficient to make vertical profiles with spatial scales of a few kpc or less.

Taken together, these observations would show how the temperature and metal content change from bubble interiors to the inner CGM. They would also provide the hot gas mass in the bubbles, as well as an estimate of the hot mass flux from the bubbles into the inner CGM. These diagnostics would constrain models of gas mixing where rivers of hot gas flowing out from H II regions meet the tides of the hot CGM.

3.1.3. *High Velocity Clouds (HVCs) — Contributed by S. Zhang*

The Milky Way's high velocity clouds (HVCs), which still have many unsolved old puzzles, have gained new vitality under the concept of the galactic ecosystem (e.g., Ramesh et al. 2023). Historically the HVCs were observed in the MW's halo through their H I emission whose velocities deviate significantly from that allowed by Galactic rotation, and thought to be a reservoir to sustain star formation in the MW (Lehner & Howk 2011).

According to the all-sky HI4PI survey, the sky coverage fraction of the HVCs with H I column density larger than 2×10^{18} cm^{-2} is about 15%, and decreases to a half for those with column density larger than 10^{19} cm^{-2} (Westmeier 2018). The large coverage is mainly caused by the major HVC complexes such as complexes A, C, M, and AC, which seem to be intricate networks of narrow H I filaments and clumps. Though distances to HVCs are generally unconstrained, based on absorption features some limits have been estimated, for e.g., a distance $\leqslant$ 10 kpc to Complex C (Wakker et al. 2007), $\leqslant$ 15 kpc to Complex GCP (Wakker et al. 2008), ~4.4 kpc to Complex WD (Peek et al. 2016), and ~150 pc to Complex M (Schmelz & Verschuur 2023), which can be in turn used to constrain the H I masses, for e.g. $\sim 10^7\,M_\odot$ for Complex C (Thom et al. 2008) or 120 $M_\odot$ for Complex M. In addition, the HVCs observed by H I may be only the tip of the iceberg due to sensitivity limitations. UV absorption line studies estimate that HVCs with temperatures greater than 10^5 K cover about 80% of the sky (Shull et al. 2009; Lockman et al. 2019).

HVCs may play an impacting role in the galactic baryon cycle with those considerable mass, and are more likely an important carrier of the complex transformation processes of multiphase gas in the CGM according to their various proposed origins. HVCs may have completely different origins. For example: a) Cold gas accreted from IGM into the Milky Way. These gas have a falling speed of 50-200 km/s, an accretion rate of about 1 $M_\odot$/yr, and interact with the gas in the galactic halo (Wakker et al. 1999, 2007; Tripp & Song 2012). b) Cold gas precipitated from the CGM gas (Maller & Bullock 2004) or even condensed from the CGM wind (Mou et al. 2023). The latter simulation shows that the clouds have similar locations and properties to HVCs in Complex C. c) Gas blown out by galactic feedback and is now being incorporated into the disk again as a fountain. These HVCs should have higher metallicities. d) Gas stripped from satellite dwarf galaxies. For example, the HVC named Smith Cloud has a clear H I head-tail structure, a size of 3 kpc, a metallicity of 0.5 solar, and is very likely to be stripped gas (e.g., Gritton et al. 2017). Moreover, Smith Cloud and its leading component in its forward direction may be an organic whole, and are interacting with the galactic disk. e) The dark matter mini-halo bounces up and down the galactic disk, and drags the ISM out (Galyardt & Shelton 2016). These are important processes in the baryon cycle that regulate the coevolution of CGM and galaxies, and thus understanding HVCs is essential for understanding the galactic ecosystem.

More interestingly, the infalling process of HVCs toward the galactic disk is accompanied by the interaction with the hot gas in the CGM (Wakker et al. 1999, 2007; Tripp & Song 2012), and forms warm-hot transition layers of 10^{5-7} K due to turbulent mixing or shock heating (Shelton et al. 2012), as revealed by the absorption features of highly ionized species in the far-UV and the X-ray band (e.g., Sembach et al. 2003; Collins et al. 2007). Trough soft X-ray absorption studies, along the sight lines to background AGNs that penetrate HVCs, the O VII *r* lines can be detected with column density of about $10^{16-18.8}$cm^{-2}, thought the blue-shifted line centers generally have large error bars (e.g., Fang et al. 2015). On the other hand, ROSAT 1/4 keV map had shown the X-ray emission from HVCs through the soft excesses (Shelton et al. 2012). The observed intensity is about 10^{-4} counts/s/arcmin^2 (or $\sim 10^{-9}$ erg/s/cm^2/sr), similar to that of the local bubble. Nevertheless, due to the limited AGN sight lines and the low spectral resolution of ROSAT, an unbiased view of HVC transition layers is currently not available.

Therefore, a census of the absorption and emission properties of HVCs will provide valuable information. HUBS with high sensitivity and spectral resolution should have the capability to reveal micro-physics in the transition layers, and significantly improve the understanding of the roles HVCs play in Galactic ecosystem.

A simulated O VII triplet demonstrates this ability (Figure 5), which consists of the diffuse X-ray background radiation from McCammon's model (McCammon et al. 2002) and the radiation from an HVC. This HVC radiation is set to have the

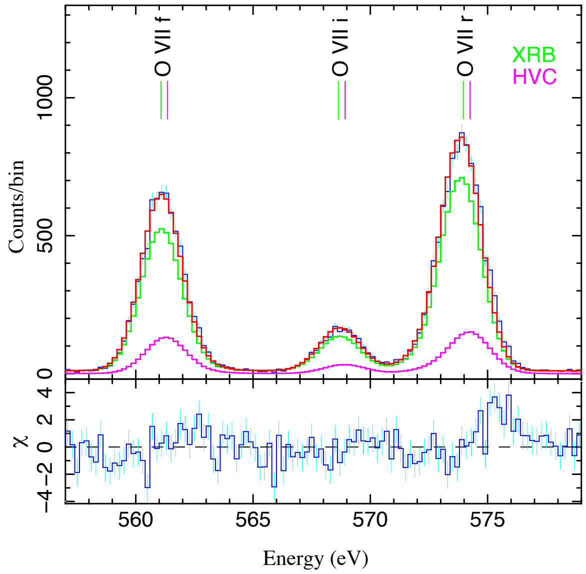

Figure 5. A simulated O VII triplet whose emission comes from the diffuse X-ray background (green) and an HVC (magenta) with a blueshifted velocity of 150 km/s. The red curve shows the best-fit model including only the background component.

same emission measure as the local bubble, 0.1 keV temperature, 0.5 solar abundance, but with a blueshifted velocity of 150 km/s. The spectrum uses all the radiation from a square degree FOV of HUBS, assuming a 20 ks exposure; but fitted only with the diffuse background model. In the apparently perfect fit, there is a clear excess in the residual at the blue wing of the O VII *r* line. This phenomenon is shown in multiple lines such as C VI and N VI, indicating the presence of a blueshifted HVC component.

• **Decomposition of HVC emission and its properties**

This configuration as shown in the figure in fact presents for a slightly difficult situation for the detection, i.e., the background cannot be effectively subtracted, and the HVC radiation has very similar properties to that of the diffuse X-ray background. According to the HI4PI survey, the velocity of HVCs is generally between 70-450 km/s; and 150 km/s is relatively small and hard to detect. Nevertheless, HUBS can discover such a velocity component, and thus performing detailed analysis and reasonable fitting of this component is feasible. For example, merely from the residual situation of the O VII *r* and *f* lines, one can realize whether the HVC radiation is emitted by hot gas or produced by charge exchange while the cold and the hot gas interact, and then perform reasonable modeling and fitting. Since the diffuse X-ray background can be separated properly, this kind of fitting can constrain the temperature and the metal abundance of the transition layer more tightly.

• **Origin and Fate**

One important reason that hinders the judgment of HVC origin is the inability to accurately determine the distance. Studies solely relying on X-ray radiation do not help much too. But HUBS's large effective area also enhances the capability to study absorption lines, allowing more sight lines to background AGNs and in turn to infer the absorption column density in the transition layer. Combined with the emission measure of the thermal emission, the volume density can be deduced and then the distance, mass, size, etc. Based on these, we can better justify the origin of HVCs. For example, the metal abundance of accreted gas should be lower, while that of feedback gas will be higher.

Another puzzle of HVCs is how they can exist for so long and accelerate to such a high speed (Zhang et al. 2017). The existence of the transition layers is considered to be closely relevant (Nelson et al. 2020). Therefore, HUBS's study can help to unravel this puzzle and predict the lifespan or fate of HVCs. Furthermore, if there is obvious CX emission, even the true velocity of HVCs relative to CGM can be derived by line ratios, and then the falling angle and the final impacting position on Galactic disk.

Generally, HUBS does not need to specifically observe HVCs, but can do so as a byproduct when observing other sources. Considering a 2-year lifetime, HUBS can observe a thousand sources with individual exposure times reaching 50 ks. According to the sky coverage rate of HVCs, about 150 sources will involve H I HVCs in the FOV, while about 800 sources will involve warm ionized HVCs. Consequently, there are ample opportunities to observe HVCs and study their transition layers with enough spatial resolution.

3.1.4. *The MW center*
— Contributed by G. Ponti

3.2. *Hot gaseous environment of nearby galaxies*

3.2.1. *Signatures of interaction of the LMC/SMC with the MW CGM*
— Contributed by Y. Faerman

3.2.2. *Diffuse X-ray emission from isolated dwarf galaxies in the Local Volume*
— Contributed by Y. Faerman

3.2.3. *Extended hot CGM around M31/M33*
— Contributed by J.-T. Li

■ Scientific justification

The Andromeda galaxy (M31), as our massive neighbor, provides us an ideal laboratory to study the extended hot CGM from the accretion of external gas. This is clearly different from the internal gas ejected by galactic feedback, which has distinguishable physical and chemical properties, as well as dependence on other galaxy parameters (§1). As one of the most massive spiral galaxies (stellar mass $M_* = 1.1 \times 10^{11}$ M$_\odot$), M31 has an extremely low SFR of only $\sim$ 0.4 M$_\odot$ yr^{-1} (Barmby et al. 2006). There will thus be little contamination to the hot CGM from current SF feedback, which often dominates the accretion component due to its high metallicity. M31 also locates in a relatively low density environment, where the IGrM of the Local Group is not as intense as in massive galaxy clusters. As the closest major galaxy ($d = 0.78$ Mpc, $1' \approx 230$ pc), we can also achieve an unparalleled spatial resolution in HUBS observations of M31, which could be comparable to *Chandra* or *XMM-Newton* observations of other external galaxies at a distance of $d > 50$ Mpc (with *Chandra*; e.g., NGC 1961; Anderson & Bregman 2011) or $d \approx 10$ Mpc (with *XMM-Newton*; e.g., NGC 891; Hodges-Kluck et al. 2018). In the mean time, we could detect objects with much lower intrinsic luminosities.

We herein justify the possibility of a moderately deep HUBS mosaic observation program covering the M31/M33 subgroup, with a FOV roughly covering the same sky area as the PAndAS survey (Richardson et al. 2011; Fig. 6). This sky area roughly covers $r \lesssim 150$ kpc $\sim 75\%$ r_{200} from M31 [$r_{200} \approx (189 - 213)$ kpc; Tamm et al. 2012] and $r \lesssim 50$ kpc $\sim 30\%$ r_{200} from M33 ($r_{200} \approx 168$ kpc; Kam et al. 2017), including the stellar and cold gas stream connecting them (Braun & Thilker 2004; Richardson et al. 2011). There are also $\sim$ 20 known dwarf galaxies covered (e.g., Richardson et al. 2011). Based on existing X-ray observations of massive quiescent spiral galaxies, the hot CGM is never detected beyond this area (e.g., Bogdán et al. 2015; Li et al. 2017a). Even with stacking analysis, the CGM is at most firmly detected to $r \sim 20\%$ r_{200} (e.g., Li et al. 2018; $r \sim 40$ kpc in the case of M31). We therefore believe the proposed HUBS observations could cover most of the interesting CGM X-ray features, while still allow for a clean local sky background subtraction. In addition to the moderately deep survey of the entire M31/M33 area, we also propose deep follow-up observations covering a few deg^2 of interesting features, such as the disk and immediate surrounding areas of M31. These deep observations, aiming at reaching full spatial resolution of HUBS at a moderate S/N, will be helpful to resolve some relatively bright extended structures.

In addition to the proposed HUBS observations, higher resolution X-ray images are also critical in detecting the X-ray point-like sources toward the direction of M31/M33 (e.g., with XMM-Newton, Huang et al. 2023a; eROSITA, Predehl et al. 2021; or in the future AXIS, Mushotzky 2018). Furthermore, there also exist extensive sets of multi-wavelength data sensitive to the extended stellar light (e.g., Richardson et al. 2011) and multi-phase gases in the CGM/IGrM. The latter includes the warm ionized gas traced by UV absorption lines

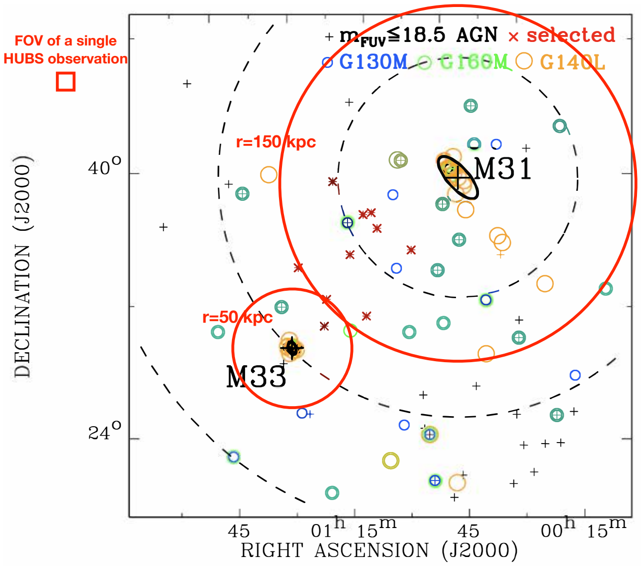

Figure 6. Location of UV bright (with GALEX FUV magnitude $m_{\rm FUV} \leq 18.5$) AGNs (black plus) around M31 and M33. The large plus sign and the solid black ellipse mark the location and extension of the optical disk of the two galaxies. The three large dashed black circles have radius of r = 100, 200, 300 kpc from the center of M31. Small colored circles as denoted on top right are HST/COS observations of objects in the surrounding area (Rao et al. 2013), or are MW halo stars which allow for a determination of the absorption from the foreground MW halo (Lehner et al. 2015). The red box on top left is the FOV of a single HUBS observation. The two solid red circles have r = 150, and 50 kpc from the center of M31 and M33, respectively, and are *roughly* the mapping area of the proposed HUBS mosaic observations.

(e.g., Lehner et al. 2020; Fig. 6) or optical emission lines (e.g., Drechsler et al. 2023), the extended cold atomic gas traced by the H I 21 cm line (e.g., Braun & Thilker 2004), as well as studies of the intervening gases via some background radio sources (radio pulsars, FRBs, etc., e.g., Prochaska & Zheng 2019). Detection of extended γ-ray emission around M31 is also claimed, which traces high-energy CRs (e.g., Ackermann et al. 2017). Based on the proposed HUBS observations and the multi-wavelength archival data toward this direction (e.g., Fig. 6), we plan to explore the following scientific problems:

• *Physical, chemical properties, and spatial distribution of the hot CGM.* With the micro-calorimeter on-board HUBS, we will reach ∼ 2 eV energy resolution, which is sufficient to resolve individual emission lines from the continuum (Fig. 7). This is completely different from the low-resolution X-ray imaging spectroscopy with CCDs. We can directly measure the physical and chemical properties of the hot CGM with little impact from the metallicity-emission measure degeneracy in the modeling of low-resolution X-ray spectra (e.g., Li et al. 2016b, 2017a). A more accurate measurement of the hot gas properties will help us to not only better estimate the total mass contained in the hot CGM, but also search for the interface between the feedback and the ambient or accreted materials, which are expected to have different metallicities and temperatures (e.g., Crain et al. 2013).

The proposed HUBS mapping area spans a DEC range of ∼ 25°, which represents a significant gradient in the MW foreground (e.g., Snowden et al. 1997; Predehl et al. 2020). After a clean subtraction of the sky background based on a few "blank-sky" region covered by the proposed observations, we will search for large-scale X-ray emission line structures such as the *eROSITA* bubble (Predehl et al. 2020). These structures are clearly predicted in numerical simulations of M31-like galaxies (e.g., Pillepich et al. 2021), but often difficult to detect with broad-band X-ray images from archival (e.g., *XMM-Newton* has a continuous coverage of only $r \lesssim 30$ kpc from M31; Huang et al. 2023a) or new shallow X-ray observations (four years *eROSITA* survey has an average depth of ∼ 1.5 ks, while the instrument sensitivity to extended sources is comparable as HUBS). Cleanly removing the sky background is also critical in quantitatively measuring the "missing baryons" contained in the hot CGM (e.g., Dai et al. 2012; Bregman et al. 2018, 2022). We will characterize the spatial distribution of the hot CGM by extracting intensity profiles of individual emission lines and extrapolating it to the virial radius (e.g., Li et al. 2018).

• *Non-thermal emission from the tidal stream.* Resolving individual emission lines in the high resolution spectra of HUBS will also help us to search for signatures of some non-thermal X-ray emissions. The relative strength of the resonance, intercombination, and forbidden lines are different in thermal and charge exchange X-ray emissions (CXE; e.g., Smith et al. 2012). The triplets of some ions (O VII, Ne IX, Mg XI) could thus be strong diagnostic features of these different processes (e.g., Liu et al. 2011). As CXE appears at the interface between cold and hot gases with relative motions, we will search for signatures of CXE from the stellar and cold gas streams connecting M31 and M33 (e.g., Braun & Thilker 2004; Richardson et al. 2011).

• *Other X-ray sources.* In addition to the large-scale CGM/IGrM, the proposed HUBS observations will also cover many other X-ray sources toward M31/M33, which could be firmly identified based on the large collection of multi-wavelength data (e.g., Huang et al. 2023a). In particular, we will search for extended X-ray emissions from dwarf galaxies and globular clusters by stacking the X-ray data toward tens of such objects (e.g., Cezario et al. 2013). Quiescent dwarf galaxies and globular clusters are typically not expected to host a hot halo, but when residing in a group, it is not impossible for them to have small amount of extended X-ray emissions via the interaction with the hot IGrM. In addition to emission lines, X-ray absorption lines in the stacked X-ray spectra of bright point-like sources (AGN, X-ray binary, pulsar, etc.) will also help us to study the hot gas in the MW halo or the IGrM between the MW and M31 (e.g., Qu et al. 2021).

■ Technical Justification

Because of its high energy resolution, large FOV, and low instrumental background, HUBS is optimized for the study of the extended X-ray emissions within the M31/M33 subgroup. We will need ~ 300 HUBS observations to cover the entire area of interest (e.g., Fig. 6). We herein estimate the requested exposure time of each observations. We assume a MW foreground from a $r = 2° - 8°$ annulus centered at M31, based on the data from the *ROSAT* all sky survey. This MW foreground spectrum can be well fitted with a two-component thermal plasma model (Fig. 7): a $kT \approx 0.18$ keV APEC model probably representing the emission from the local hot bubble (LHB), and a multi-temperature plasma emission model (gadem) with a mean temperature of $kT \approx 0.72$ keV probably representing the emission from the MW halo. This MW foreground model will be fixed and rescaled (to the real spectral extraction aperture size) in the follow-up simulations.

Due to its low angular resolution, contamination from unresolved point-like X-ray sources could be important, including either various types of foreground or local stellar sources, or largely the background AGN. Adopting the stellar source number density and luminosity function in the inner halo of M31 (outside the galactic disk) from the New-ANGELS survey (with *XMM-Newton*; Huang et al. 2023a, we estimate the total 0.5-2 keV contribution from X-ray point sources as $\sim 10^{39}$ ergs s^{-1} deg^{-2}. This is about one order of magnitude higher than the MW foreground in the HUBS energy range, but typically has a featureless continuum with no prominent emission lines (assuming a $\Gamma = 1.8$ power law model; Fig. 7) so not difficult to subtract.

The strength of the extended X-ray emission from the hot CGM or IGrM around M31/M33 is quite uncertain, as it is not yet firmly detected. The non-detection is largely caused by the small sky area covered by the existing *Chandra* or *XMM-Newton* observations (e.g., Huang et al. 2023a), or the shallow exposure in X-ray all sky surveys (*ROSAT* or *eROSITA*). Nevertheless, some enhanced line emissions toward the direction of M31 (at $r \lesssim 20°$) have been revealed based on a large collection of archival data over the entire sky (e.g., Qu et al. 2021). Assuming the X-ray luminosity of the hot CGM of M31 is comparable to some other comparably massive and quiescent isolated spiral galaxies (e.g., Li et al. 2017a), we obtain the total expected 0.5-2 keV luminosity of the hot CGM of M31: $L_X \sim 10^{39.3-40.3}$ ergs s^{-1}. We herein conservatively assume $L_X \sim 3\times10^{39}$ ergs s^{-1}. If the X-ray emission is uniformly distributed within $r \lesssim 4^\circ \sim 50$ kpc, the average diffuse X-ray emission from the hot CGM/IGrM will be about one order of magnitude lower than the MW foreground (Fig. 7a,b). This is typically the faintest extended features we can firmly detect with a careful characterization and subtraction of the local sky background (e.g., Li et al. 2017a, 2018).

We simulate the spectra extracted from an entire HUBS $1^\circ \times 1^\circ$ FOV based on the above MW foreground, point-like X-ray sources, and hot CGM/IGrM emission models [assuming a $kT \sim$ 0.75 keV solar abundance thermal plasma model (APEC) model]. With $\sim$ 10 ks exposure time, we can collect $\sim 10^5$ counts from a single HUBS FOV, but only $\sim$ 3% are from the hot CGM/IGrM component. If a reliable local background can be modeled and subtracted (so all the background models can be fixed), we can measure the temperature and normalization of the hot gas component to an accuracy of $\sim$ 7% and $\sim$ 16% (90% confidence level), respectively, but the metallicity cannot be well constrained.

In the above estimates, we assume there is no resolvable extended hot gas features. However, such features at different physical scales have been detected in many nearby galaxies (e.g., Strickland et al. 2004a; Li et al. 2008; Li & Wang 2013a; Li et al. 2019; Hodges-Kluck et al. 2020), which could be significantly X-ray brighter and easier to detect. If we assume such an extended hot gas structure has a mean surface brightness about one order of magnitude higher than the hot CGM/IGrM component adopted above and the structure is still large scale (larger than the FOV of HUBS), the X-ray photons from the hot halo gas component will be $\sim$ 25% of the total value (Fig. 7c,d). Individual emission lines can be well resolved in the X-ray spectra, although still highly blended with the MW foreground components. Again with a fixed background model, we can now roughly constrain the metallicity of the hot gas to an accuracy of $\sim$ 40% at 90% confidence level.

If there are some finer structures with a physical scale much smaller than the FOV of HUBS, we will need a much deeper observation to collect sufficient number of photons in each HUBS normal pixel. Here we simulate HUBS spectra with an exposure time of $\sim$ 300 ks, for a $1'$ feature with a surface brightness $\sim$ 3 (Fig. 7e) or 10 times (Fig. 7f) higher than those in the above case (Fig. 7c,d). We can collect $\sim$ 1500 ($\sim$ 3200) counts in Fig. 7e (Fig. 7f) and roughly constrain the temperature and metallicity of the hot gas to an accuracy of $\sim$ 4% and $\sim$ 70% ($\sim$ 2% and $\sim$ 36%) in each pixel. This will enable spatially resolved mapping of the hot gas properties or some individual emission lines at the full angular resolution of HUBS. Such deep observations are only needed in some selected regions with prominent soft X-ray features (e.g., the possible superbubble). We anticipate only $\sim 3-4$ FOVs need such deep observations. **The total requested HUBS observation time for both the wide shallow survey** ($\sim 300\times10$ ks) **and the deep follow-up of selected FOVs [**$\sim (3-4)\times300$ ks**] are** $\sim$ 4 Ms**.**

3.2.4. *Hot CGM around the most massive isolated spiral galaxies — Contributed by J.-T. Li*

■ Scientific justification

The high energy resolution of *HUBS* is not only critical in studying the physical, chemical, and dynamical properties of the hot CGM, but also critical in narrow-band imaging separating prominent emission lines from the CGM of nearby galaxies and the MW halo. This will greatly reduce the sky background (actually dominated by the foreground), and enable us to probe the hot CGM distribution to a large radial range from the galactic center (e.g., Fig. 8; Li 2020). Well constraining the hot CGM distribution within the dark matter halo further helps us to quantitatively estimate the baryon

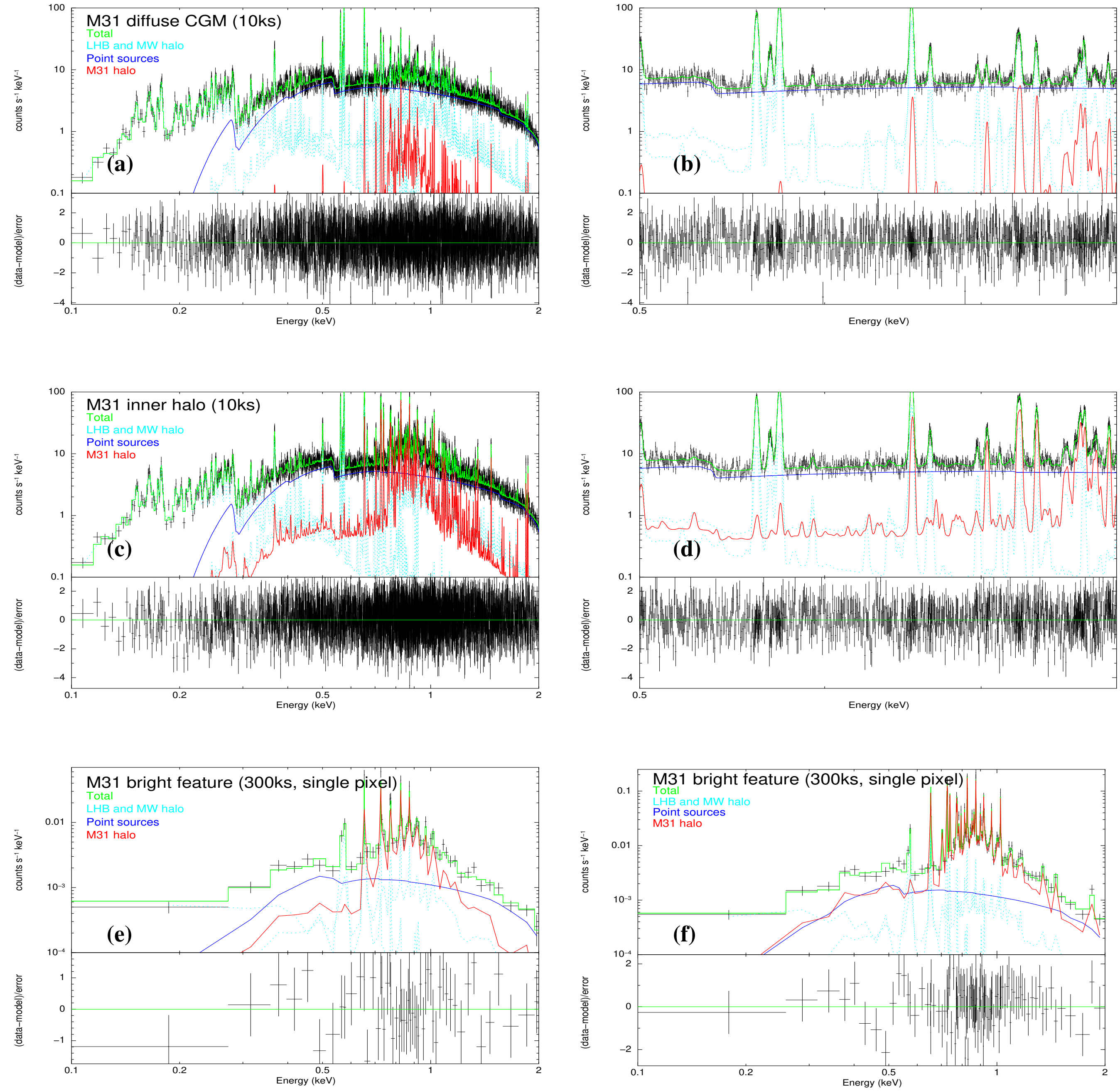

Figure 7. Simulated HUBS spectra extracted from M31 halo. The green curve is a sum of different model components, and is a best-fit to the black data points. The cyan curves are the contributions from the local hot bubble (LHB; dominates the soft X-ray band at $\lesssim$ 0.4 keV) and the MW halo (dominates at $\gtrsim$ 0.4 keV). The blue curve is the point source contribution, including both foreground and M31 local stellar sources, as well as distance AGN. The red curve is the emission from the hot gas in the M31 halo. The top row is the simulated 10 ks HUBS spectrum extracted from a $\sim 1^\circ$-diameter aperture in the M31 halo, assuming the expected hot CGM emission is uniformly distributed at $r \lesssim 4^\circ \sim$ 50 kpc. Panel (b) is a zoom-in of panel (a) in the energy range of 0.5-0.8 keV. The middle row is similar as the top row, but here we assume the hot CGM component is about one order of magnitude brighter. This simulation thus represents the average flux density of the hot CGM at $r \lesssim 1.2^\circ \sim$ 15 kpc. The two panels in the bottom row are the simulated spectra of some bright diffuse X-ray features, with a flux density ~ 3 or ~ 10 times of the average value at $r \lesssim 1.2^\circ \sim$ 15 kpc. Here the spectra are extracted from a single $\sim 1'$ pixel of the HUBS normal array, instead of the entire $\sim 1^\circ$ FOV such as in the top and middle row.

budget of the galaxy (e.g., Li et al. 2018; Bregman et al. 2018, 2022).

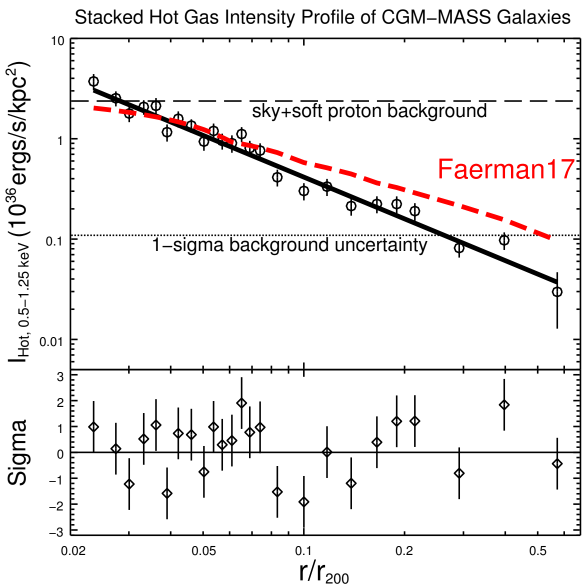

Figure 8. Stacked radial X-ray intensity profile of the hot gas around a sample of massive isolated spiral galaxies (the CGM-MASS sample; Li et al. 2016c, 2017a, 2018; Li 2020). The radial distance of different galaxies has been rescaled to r_{200}. The solid line is the best-fit β-function. The dashed and dotted lines show the sky+soft proton background and the 1-σ uncertainty. The red dashed curve is the model from Faerman et al. (2017) scaled to r_{200} of a MW-sized halo.

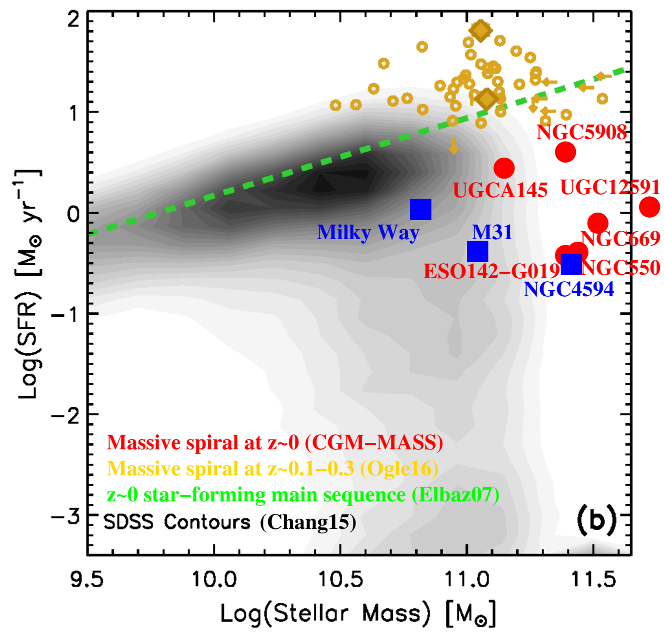

Figure 9. Comparing massive spiral galaxies to other galaxy populations on the SFR-M_* diagram. Red circles are the CGM-MASS galaxies proposed for *HUBS* observations. They are extremely massive and quiescent. Blue boxes are the Milky Way and two other well known massive quiescent spirals in the local Universe (M31 and NGC 4594). Gold symbols are the "super spirals" at $z \sim 0.1-0.3$ from Ogle et al. (2016), which may be progenitors of the extremely massive quiescent spirals at $z \sim 0$. Green dashed line is the star-forming main sequence at $z \sim 0$ (Elbaz et al. 2007). Galaxies below this line have growth times longer than the Hubble time under the current SFR. Grey contours are Chang et al. (2015)'s SDSS-WISE sample.

Compared to star forming galaxies or quiescent elliptical galaxies, massive isolated quiescent spiral galaxies provide us with a clean environment to study the hot CGM, with little contamination from the metal enriched feedback material or the intra-group/intra-cluster medium (IrGM, ICM). These galaxies could also be massive enough, so the accreted external gas could be virialized and heated to an X-ray emitting temperature (e.g., White & Frenk 1991; Kereš et al. 2005). Studying the hot CGM distribution thus also tells us how the external gas reservior was accreted and feed the SF in the galactic disk.

The high energy resolution and large FOV of the micro-calorimeter on board *HUBS* make it optimized for the study of the extended faint hot CGM around massive galaxies (e.g., Li 2020). We herein propose a *HUBS* deep survey of a small sample of $\sim$ 10 massive spiral galaxies typically located at a distance of $d = 50-100$ Mpc, similar as the CGM-MASS sample studied in Li et al. (2016c, 2017a, 2018). This science case has been briefly described in Bregman et al. (2023), while we introduce it in more details here. The CGM-MASS sample is selected from the giant spirals in the luminosity class range of LC I-III (supergiant to normal giant) from NED, with the following criteria (Li et al. 2016c, 2017a): (1) the apparent maximum gas rotation velocity $v_{\rm maxg} \gtrsim 300$ km s^{-1}; (2) Galactic foreground absorption column density $N_H < 10^{21}$ cm^{-2}; (3) distance $d < 100$ Mpc; (4) stellar mass $M_* \gtrsim 1.5 \times 10^{11} {\rm M_\odot}$; (5) SFR$/M_* < 0.5\ {\rm M_\odot yr^{-1}}/(10^{10}{\rm M_\odot})$. For galaxies passing these criteria, we finalize our selection by checking their optical images within 30′ ($\sim$ 600 kpc at a distance of 70 Mpc) around each galaxy, and select only those with no bright companions. There are in total six galaxies in the CGM-MASS sample (e.g., Fig. 9), plus a few similar but more face-on ones (so have smaller $v_{\rm maxg}$ but the inclination corrected velocity $v_{\rm rot}$ is still large enough; e.g., Anderson & Bregman 2011; Anderson et al. 2016; Bogdán et al. 2013), in total $\sim$ 10 galaxies in the final sample. These galaxies are the best laboratories to study the (especially accreted) hot CGM properties and distribution in isolation.

At a distance of $d \sim 50-100$ Mpc, or a redshift of $z \sim 0.01-0.02$, prominent soft X-ray emission lines tracing the hot CGM, e.g., O VII at $\sim$ 0.666 keV and O VIII at $\sim$ 0.654 keV, can be separated from the same lines produced in the MW halo with the $E/\Delta E \sim 500$ energy resolution of *HUBS* (Fig. 10; §2). At this distance, the $\sim 1°$ FOV of *HUBS* corresponds to $\sim 900-1800$ kpc, while the virial radius of the CGM-MASS galaxies is typically $r_{200} \sim 350-600$ kpc, so we typically only need a single *HUBS* exposure per galaxy to cover its entire dark matter halo. With the proposed deep *HUBS* observations of these nearby massive isolated spiral galaxies, we can examine the following specific science: (1) Detect the faint CGM signal at the outskirt of the dark matter halo and characterize the spatial distribution of the hot CGM over a large radial range (e.g., Li et al. 2018). This will help us to quantitatively measure the hot baryon content of a galaxy with little uncertainties based on the extrapolation of the observed X-ray intensity profile with current X-ray CCD detectors. (2) Measure the metallicity of the CGM at different radial ranges (e.g., Anderson et al. 2016). The metallicity traces the metal enrichment processes, mainly by the galactic feedback. It is thus critical to search for the interface between the metal-poor accreted material and the metal-rich feedback material, and further examine if the externally accreted gas can be virialized only via gravitational heating. (3) Calculate the radiative cooling timescale $t_{\rm cool}$ at different radius (e.g., Li et al. 2017a). This further helps us to determine the cooling radius $r_{\rm cool}$, within which the hot CGM could cool within the Hubble time. We can further study the radial variation of the ratio $t_{\rm cool}/t_{\rm ff}$, where $t_{\rm ff}$ is the free fall timescale. This ratio determines the thermodynamics of the hot CGM and the presence of multi-phase gas within the galactic halo (e.g., Voit & Donahue 2015).

■ Technical Justification

We make technical justifications of the proposed *HUBS* observations of massive isolated spiral galaxies based on a model template constructed from the CGM-MASS sample (Li et al. 2017a, 2018; Li 2020). The model includes only the hot CGM emission ($kT \sim 0.6$ keV, using parameters similar as NGC 5908 in the CGM-MASS sample; Li et al. 2016c) plus various sky background components: the low-temperature local hot bubble (LHB), the non-thermal cosmic background mostly from distant AGN, and the MW halo. At the current stage, we do not add an instrument background component. We also do not add an AGN component from the host galaxy, the residual from which often presents due to the poor subtraction of it with the low-angular resolution of *HUBS*, but this featureless component should not strongly impact our study of the emission lines from hot gas.

As shown in Fig. 10, within $\sim$ 1 Ms exposure, we can collect sufficient number of photons from the hot CGM at $r \leq 0.2r_{200}$ around a massive spiral galaxy at $z = 0.01$ ($d \sim 50$ Mpc), in order to resolve some key diagnostic emission lines of the hot gas. These lines are redshifted from the same lines in the MW halo, which are the strongest contaminating source in low-resolution X-ray imaging

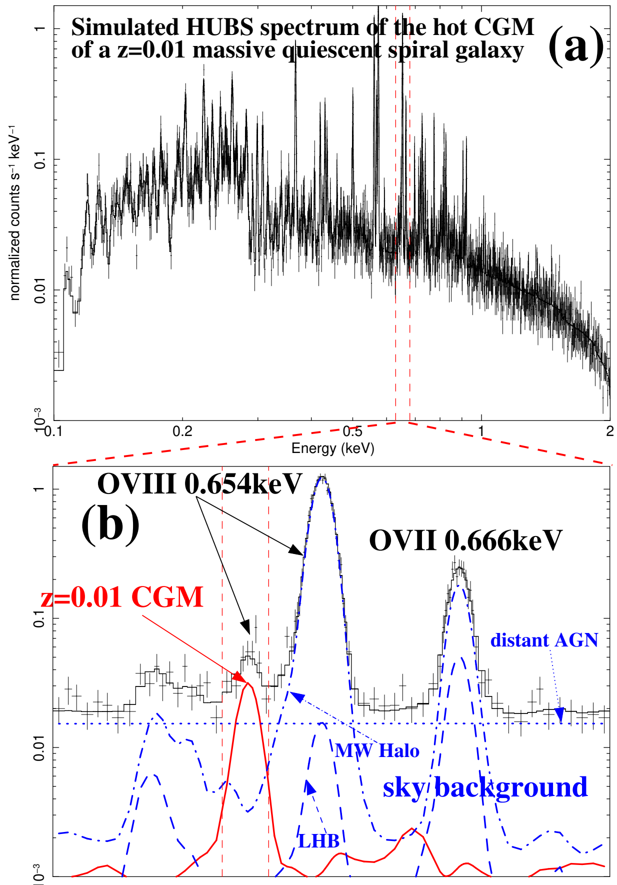

Figure 10. A simulated 1 Ms HUBS spectrum of the hot CGM at $r \leq 0.2r_{200}$ around a $z = 0.01$ ($d \sim 50$ Mpc) galaxy, showing the importance of narrow-band imaging in removing the MW foreground (Li 2020; Bregman et al. 2023). Instrument background components are not added. Panel (b) is the zoom-in in the energy range of 0.63–0.68 keV of panel (a). The red curve is the hot CGM ($kT = 0.6$ keV plasma), while the blue curves are various sky background components (local hot bubble LHB; MW halo; distant AGN). The redshifted O VIII line from the CGM can be separated from the MW halo component.

spectroscopy observations (e.g., Li et al. 2017a). When probing X-ray emission from low surface brightness features such as the extended CGM, the most important thing is often not only the photon statistic, but also the level and fluctuation of the sky background, and the strongest background component in narrow bands covering the key diagnostic lines is often the MW foreground (e.g., Li et al. 2018). Separating the hot CGM emission from the MW foreground in spectroscopy and narrow-band imaging observations thus significantly increase the signal-to-noise ratio in detecting faint features. This provides us the best way (narrow-band imaging of the lines) to probe the hot CGM distribution at large galactocentric radii.

The above justification is only an order-of-magnitude estimate of the required exposure time and certainly oversimplified, just giving the readers a sense that *HUBS* could detect the extended faint hot CGM in a nearby galaxy with $\sim$ Ms exposures. The real adopted galaxy sample could be different, which strongly affect the required exposure time. The redshift and distance of the objects in such observations need to be carefully adjusted. A lower distance will be helpful to collect more photons, but the contamination from the MW foreground can be stronger. On the other hand, a too large distance will significantly reduce the flux of the object and makes the project unfeasible. The best choice will be objects at $d \sim (50-100)$ Mpc, such as the galaxies proposed for this study, although other projects could certainly choose galaxy samples with different criteria. We also would like to emphasize that the galaxies in the mass range of the CGM-MASS galaxies often have a large discrepancy in the measured hot CGM mass based on X-ray or SZ observations (e.g., Bregman et al. 2022), which could be partially caused by the poorly constrained hot gas density profile (e.g., Bogdán et al. 2015; Li et al. 2018). This is another reason to have deep X-ray observations probing the hot CGM distributed in a large fraction of the dark matter halo. The total HUBS observation time needed to complete a survey as proposed in this section will be **a few mega-seconds**, depending on the real sample size and the adjustment of the exposure time for individual galaxies based on existing *Chandra* and *XMM-Newton* observations (e.g., Bogdán et al. 2013, 2015; Anderson et al. 2016; Li et al. 2017a).

3.2.5. *Microphysics of the hot galactic superwind — Contributed by ?*

Volunteers?

3.3. *AGN and its feedback*

3.3.1. *The multi-scale, multi-phase AGN outflow — Contributed by ?*

Already a nice science case in the Chinese whitepaper.

Volunteers?

Huanian Zhang: I could write some phenomena of the signatures of AGN feedback.

3.3.2. *Tidal Disruption Events — Contributed by X. Shu*

■ Scientific justification

The detection of a rapidly growing number of stellar tidal disruption events (TDEs) marks a breakthrough in transient research during the past decade. A TDE occurs when a star wanders too close to a supermassive black hole (SMBH) residing in the center of a galaxy, and it can be violently ripped apart by the SMBH's strong tidal force (e.g., Rees 1988). As a result, about half of the disrupted stellar debris eventually falls back and accretes onto the SMBH, producing a bright flare of electromagnetic radiation that can last on timescales of months to years.

The TDE flares contain vital information about the disruption and can be used to constrain the properties of the SMBH as well as the disrupted star. The unique impulse of accretion produced by TDE provides evidence for the existence of a SMBH in an otherwise quiescent galaxy. Furthermore, TDEs provide an effective way to discover intermediate-mass black holes (IMBHs) with masses of $10^2 - 10^5 M_\odot$ (Lin et al. 2018) and more exotic accretion systems such as SMBH binaries (Liu et al. 2014; Shu et al. 2020). Hence, TDEs can constrain the occupation fractions of black holes in various types and masses of galaxies, which is essential for understanding the formation and evolution of galaxies and SMBHs. In addition, TDEs serve as an ideal laboratory to probe the accretion physics of SMBHs, such as super-Eddington accretion phase where winds and outflows are expected to be launched (Jiang et al. 2014; Dai et al. 2018), and even witness the formation of relativistic jets (e.g., Burrows et al. 2011; Andreoni et al. 2022).

While TDEs were firstly identified in the X-ray bands in the late 1990s, optical time-domain surveys currently dominate the discovery of TDEs and about dozens of candidates have been found to date (see recent review of Gezari 2021). In particular, the ZTF survey has boosted the discovery rate of TDEs from $\lesssim 2$ to >10 per year, opening up a new era of population studies (van Velzen et al. 2021; Yao et al. 2023). However, only a handful of optically selected TDEs have received sensitive X-ray follow-up observations and show diversities in their X-ray emission. It is still an open question for the emission mechanism of TDEs (Piran et al. 2015; Metzger & Stone 2016; Dai et al. 2018). In addition, the observed total energy released after tidal disruption is one to two orders of magnitude lower than theoretical prediction, leading to the "missing energy" puzzle. This discrepancy could be explained by the scenario that the majority of the energy released is in the extreme-UV band and/or in the form of off-axis jets/outflows (Lu & Kumar 2018). The detection and characterization of TDE outflows offers an unprecedented opportunity to tackle these unsettled questions.

Although theoretically predicted, very few TDEs have shown the evidence of outflows in their X-ray spectra so far. Flows of hot, ionized gas has been detected in the high-resolution X-ray spectra of the nearby TDE ASASSN-14li (Miller et al. 2015), with modest velocity of a few hundred km s^{-1} and a low volume filling factor from narrow linewidths. Variability in the absorption lines indicates that the gas is relatively close to the black hole. These observational properties suggest that the gas flow could be associated with either a rotating wind from a super-Eddington accretion disk, or with a filament of disrupted stellar debris near to the apocentre of an elliptical orbit. The X-rays from ASSASN-14li are also absorbed by a high-velocity wind of ~0.2 c (Kara et al. 2018), but is only evident at early times and is not seen in the observations taken about one year after the peak luminosity. The physical connections between the low-velocity gas and the fast outflows are not clear. With the superb spectral resolution and sensitivity offered by HUBS observations, our understanding of gas flows in TDEs can be improved significantly. In addition, we could explore whether the X-ray outflows are ubiquitous in TDEs which is crucial to test models for super-Edditiong accretion.

• *Characterizing flows of X-ray gas.* Because of the low spectral resolution and sensitivity of most of the X-ray imaging spectroscopy observations, it is often difficult to characterize the blueshifted absorption features when the spectral S/N is not high, leaving the physical conditions of hot, ionized gas poorly constrained. The $\sim$2 eV energy resolution provided by HUBS will enable to detect and resolve individual absorption lines. By performing the photoionization modelling using the XSTAR code (Kallman & Bautista 2001), we can determine the key physical parameters of the gas outflows, such as the velocity, ionization parameter and column density. A more accurate measurement of the outflow properties will help us to better estimate the mass outflow rate as well as the total energy carried away by outflows, which can help to solve the "missing energy" puzzle in TDEs. Meanwhile, we can constrain the feedback effect of outflows onto host's star-formation activities.

• *Constraining the chemical composition of the disrupted star.*

The shape of light curves (rise, peak and decay of the TDE flares) is directly linked to the rate of debris mass return to SMBH, which is dependent of the internal structures of disrupted stars (Lodato et al. 2015). Many numerical studies have assumed that the debris has Solar composition with a single structural profile. This might not be true as tidal disruptions should commonly involve evolved main-sequence stars (e.g., Arcavi et al. 2014). In particular, the star becomes steadily more helium rich as it evolves (Gezari et al. 2012). Hydrogen burning in the process of CNO cycle also modifies carbon, nitrogen and oxygen abundances, leading to the reduction in the amount of carbon and increase in the amount of nitrogen. In a TDE, some of the debris will have abundances and metallicities that are never observed in stellar atmospheres or the interstellar medium (Kochanek 2016), because material processed by nuclear reactions can be revealed without the need to wait for late phases of stellar evolution. Abundance anomalies is a unique property of TDEs, and might serve as a tell-tale marker to distinguish a TDE from other imposters such as AGN variability. In addition, the flux ratio variability of lines with similar ionization potentials can be used to infer the abundance evolution. The timescale for chemical enrichment can thus provide a direct observational test of which stars are being disrupted by the central SMBH (Gallegos-Garcia et al. 2018). Indeed, several TDEs display a unique ultraviolet (UV) emission-line spectrum, characterized by strong nitrogen lines and weak carbon lines, distinct from those of AGNs (Cenko et al. 2016; Yang et al. 2017; Sheng et al. 2021). With HUBS observations, we can search for abundance anomalies in the X-ray spectra of TDEs, which have not been observed yet.

• *Mapping out debris stream.* With the XMM/RGS high resolution X-ray spectroscopy observations, highly ionized gas with narrow line widths has been detected in the TDE ASASSN-14li, which were interpreted as absorption through stellar debris filament or super-Eddington disk wind (Miller et al. 2015). The absorption by debris filaments requires special geometry while super-Eddington disk wind cannot explain the low velocity or low column density inferred from the photoionization calculations. Variability in the absorption lines, i.e., flux, equivalent width, energy and velocity width, will be crucial to uncover the origin of ionized gas. Particularly, the upper limit on the radius of the absorbing gas can be constrained by the time interval of the variability, namely $r \lesssim c\delta t$. Hence, high resolution spectroscopy observations can allow for mapping out debris stream. Smaller debris stream indicates a more compact star or larger penetration parameter. In the framework of the super-Eddington disk wind, some simulations have predicted higher outflow speeds in an initial super-Eddington disk, and lower outflow speeds in a subsequent thin disk accretion (e.g., Strubbe & Quataert 2011). Future HUBS observations of new TDEs can test whether outflows associated with super-Eddington disk are ubiquitous, which can help to explain the origin of the optical emission in TDEs through the reprocessing scenario.

■ Technical Justification

X-ray observations of TDEs have shown supersoft X-ray spectra, i.e., without signficant emission above ∼2 keV, likely being dominated by thermal emission from a transient accretion disk. This makes HUBS very suitable to observe TDEs, especially in light of its high spectral resolution and sensitivity in the soft X-ray bands. As we mentioned above, only one TDE (ASASSN-14li) had X-ray grating spectroscopy observations (XMM/RGS and Chandra/LETGs) with sufficient S/N, and time-resolved spectroscopic studies have been very limited to date. With on-going eROSITA and planed EP time-domain surveys (e.g., Sazonov et al. 2021; Yuan et al. 2018) , more X-ray TDEs will be revealed in the rising to peak phase. For a typical TDE at D <100 Mpc, the peak X-ray luminosity is $L_{0.3-2\mathrm{keV}} \sim 10^{43}$ erg s^{-1}, corresponding to an X-ray flux of $\sim 10^{-11}$ erg s^{-1} cm^{-2}. In Fig. 11, we simulated the HUBS spectrum of a TDE at $z = 0.02$, using the models described in Lin et al. (2015), with an exposure of 100 ks, for an X-ray flux of $\sim 10^{-11}$ erg s^{-1} cm^{-2} and $\sim 10^{-12}$ erg s^{-1} cm^{-2}, respectively. The strongest absorption lines consistent with ionized charge states of N, O, S, and Fe, are clearly revealed, even for the lower flux level assumed. Hence, HUBS observations with a few 100ks exposures for a given TDE will enable time-resolved spectroscopic studies. This will provide an unprecedented view of the changing outflows with varying accretion rates. The same absorption spectra can also provide insight into the chemical composition and type of the disrupted star. To observe five X-ray bright TDEs as an exploratory program, we need a total of HUBS time of ∼1 Ms.

3.3.3. *More science cases on AGN*
— Contributed by ?

Volunteers? Please add more science cases on AGN

ACKNOWLEDGEMENTS

The HUBS Galactic Ecosystems SWG would like to acknowledge the HUBS PI Prof. Wei Cui and the HUBS technical supporting team for their helpful discussions. We also acknowledge the contributions from a few previous members of the SWG, who have left or joined other SWGs, including Drs. Marat Gilfanov, Aurora Simionescu, and Ekta Patel. *GP acknowledges financial support from the European Research Council (ERC) under the European Union's Horizon 2020 research and innovation program "HotMilk" (grant agreement No. 865637) and support from Bando per il Finanziamento della Ricerca Fondamentale 2022 dell'Istituto Nazionale di Astrofisica (INAF): GO Large program*

REFERENCES

Ackermann M., et al., 2017, ApJ, 836, 208
Anders E., Grevesse N., 1989, GeoCoA, 53, 197
Anderson M. E., Bregman J. N., 2011, ApJ, 737, 22
Anderson M. E., Bregman J. N., Dai X., 2013, ApJ, 762, 106
Anderson M. E., Churazov E., Bregman J. N., 2016, MNRAS, 455, 227
Andreoni I., et al., 2022, Nature, 612, 430
Arcavi I., et al., 2014, ApJ, 793, 38
Armillotta L., Fraternali F., Marinacci F., 2016, MNRAS, 462, 4157
Babyk I. V., McNamara B. R., Nulsen P. E. J., Hogan M. T., Vantyghem A. N., Russell H. R., Pulido F. A., Edge A. C., 2018, ApJ, 857, 32

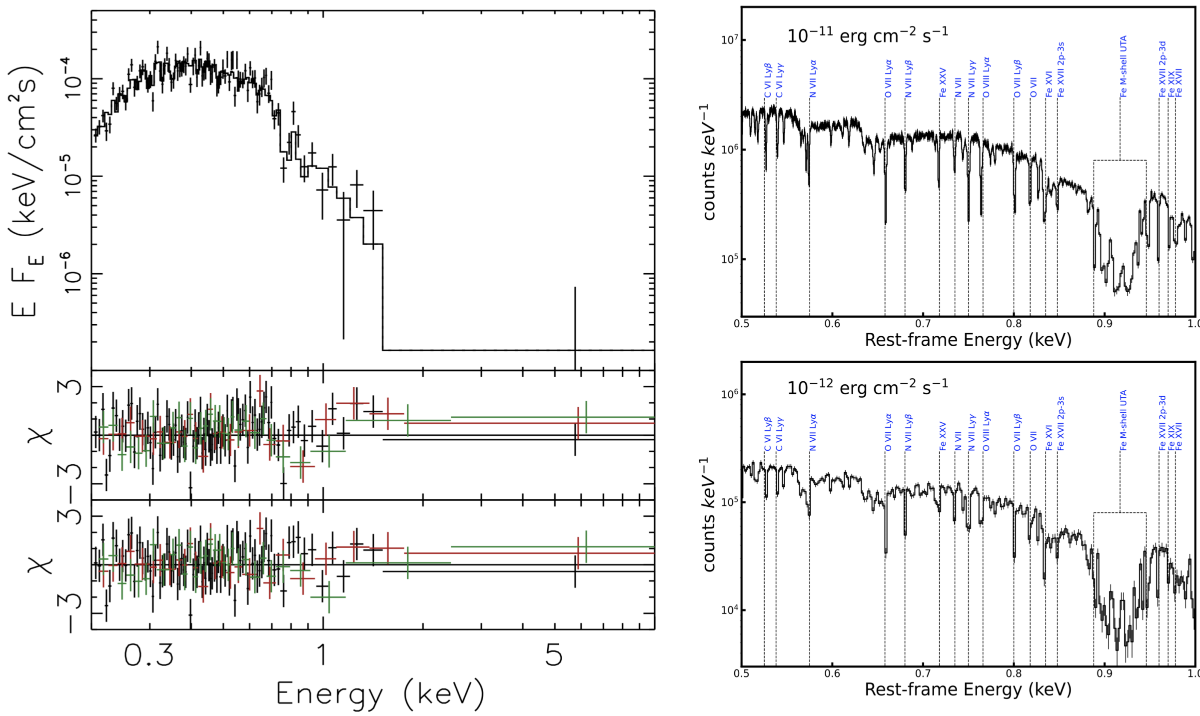

Figure 11. *Left panel:* The unfolded XMM/PN spectrum of the TDE 3XMM J152130.7+074916 with an X-ray flux of $\sim 10^{-12}$ erg s^{-1} cm^{-2} (Lin et al. 2015). The spectrum was fitted with the blackbody model subject to a fast-moving absorber with a velocity of 0.12 c (solid line). The fit residuals with the blackbody model without and with the absorber are shown in the bottom sub-panels. *Right panel:* Simulated HUBS spectrum with an exposure of 100 ks, for an X-ray flux of $\sim 10^{-11}$ erg s^{-1} cm^{-2} and $\sim 10^{-12}$ erg s^{-1} cm^{-2}, respectively.

Barmby P., et al., 2006, ApJL, 650, L45
Beck R., 2012, SSRv, 166, 215
Bell E. F., McIntosh D. H., Katz N., Weinberg M. D., 2003, ApJS, 149, 289
Benson A. J., Bower R. G., Frenk C. S., White S. D. M., 2000, MNRAS, 314, 557
Bluem J., et al., 2022, ApJ, 936, 72
Boettcher E., Zweibel E. G., Gallagher J. S. I., Benjamin R. A., 2016, ApJ, 832, 118
Bogdán Á., et al., 2013, ApJ, 772, 97
Bogdán Á., et al., 2015, ApJ, 804, 72
Boroson B., Kim D.-W., Fabbiano G., 2011, ApJ, 729, 12
Braun R., Thilker D. A., 2004, A&A, 417, 421
Bregman J. N., 1980, ApJ, 236, 577
Bregman J. N., 2007, ARA&A, 45, 221
Bregman J. N., Lloyd-Davies E. J., 2007, ApJ, 669, 990
Bregman J. N., Anderson M. E., Miller M. J., Hodges-Kluck E., Dai X., Li J.-T., Li Y., Qu Z., 2018, ApJ, 862, 3
Bregman J. N., Hodges-Kluck E., Qu Z., Pratt C., Li J.-T., Yun Y., 2022, ApJ, 928, 14
Bregman J., et al., 2023, arXiv e-prints, p. arXiv:2307.05672
Burrows D. N., et al., 2011, Nature, 476, 421
Butsky I. S., Fielding D. B., Hayward C. C., Hummels C. B., Quinn T. R., Werk J. K., 2020, ApJ, 903, 77
Cabot S. H. C., Wang Q. D., Yao Y., 2013, MNRAS, 431, 511
Cenko S. B., et al., 2016, ApJL, 818, L32
Cezario E., Coelho P. R. T., Alves-Brito A., Forbes D. A., Brodie J. P., 2013, A&A, 549, A60
Chang Y.-Y., van der Wel A., da Cunha E., Rix H.-W., 2015, ApJS, 219, 8
Collins J. A., Shull J. M., Giroux M. L., 2007, ApJ, 657, 271
Crain R. A., McCarthy I. G., Frenk C. S., Theuns T., Schaye J., 2010, MNRAS, 407, 1403
Crain R. A., McCarthy I. G., Schaye J., Theuns T., Frenk C. S., 2013, MNRAS, 432, 3005
Cui W., et al., 2020, in Society of Photo-Optical Instrumentation Engineers (SPIE) Conference Series. p. 114442S (arXiv:2101.05587), doi:10.1117/12.2560871

Dai X., Anderson M. E., Bregman J. N., Miller J. M., 2012, ApJ, 755, 107
Dai L., McKinney J. C., Roth N., Ramirez-Ruiz E., Miller M. C., 2018, ApJL, 859, L20
Das S., Mathur S., Nicastro F., Krongold Y., 2019a, ApJL, 882, L23
Das S., Mathur S., Gupta A., Nicastro F., Krongold Y., 2019b, ApJ, 887, 257
Donahue M., Voit G. M., 2022, PhR, 973, 1
Drechsler M., et al., 2023, Research Notes of the American Astronomical Society, 7, 1
Elbaz D., et al., 2007, A&A, 468, 33
Ezoe Y., Kokubun M., Makishima K., Sekimoto Y., Matsuzaki K., 2006, ApJ, 638, 860
Fabbiano G., 1989, ARA&A, 27, 87
Faerman Y., Sternberg A., McKee C. F., 2017, ApJ, 835, 52
Faerman Y., Sternberg A., McKee C. F., 2020, ApJ, 893, 82
Fang T., Mckee C. F., Canizares C. R., Wolfire M., 2006, ApJ, 644, 174
Fang T., Buote D., Bullock J., Ma R., 2015, ApJS, 217, 21
Forman W., Jones C., 1982, ARA&A, 20, 547
Forman W., Jones C., Tucker W., 1985, ApJ, 293, 102
Fox A. J., et al., 2014, ApJ, 787, 147
Fox A. J., et al., 2015, ApJL, 799, L7
Fraternali F., van Moorsel G., Sancisi R., Oosterloo T., 2002, AJ, 123, 3124
Fukazawa Y., Botoya-Nonesa J. G., Pu J., Ohto A., Kawano N., 2006, ApJ, 636, 698
Fuller C. A., Kaaret P., Bluem J., Kuntz K. D., Hodges-Kluck E., Jahoda K. M., 2023, ApJ, 943, 61
Gallegos-Garcia M., Law-Smith J., Ramirez-Ruiz E., 2018, ApJ, 857, 109
Galyardt J., Shelton R. L., 2016, ApJL, 816, L18
Gezari S., 2021, ARA&A, 59, 21
Gezari S., et al., 2012, Nature, 485, 217
Gritton J. A., Shelton R. L., Galyardt J. E., 2017, ApJ, 842, 102
Gupta A., Mathur S., Krongold Y., Nicastro F., Galeazzi M., 2012, ApJL, 756, L8
Haffner L. M., Reynolds R. J., Tufte S. L., Madsen G. J., Jaehnig K. P., Percival J. W., 2003, ApJS, 149, 405
Han J. L., Manchester R. N., Qiao G. J., 1999, MNRAS, 306, 371
Han J. L., Manchester R. N., van Straten W., Demorest P., 2018, ApJS, 234, 11
Han J. L., et al., 2021, Research in Astronomy and Astrophysics, 21, 107
Heald G., et al., 2011a, A&A, 526, A118
Heald G., et al., 2011b, A&A, 526, A118
Heiles C., Haffner L. M., Reynolds R. J., 1999, in Taylor A. R., Landecker T. L., Joncas G., eds, Astronomical Society of the Pacific Conference Series Vol. 168, New Perspectives on the Interstellar Medium. p. 211
Henley D. B., Shelton R. L., 2012, ApJS, 202, 14
Henley D. B., Shelton R. L., 2013, ApJ, 773, 92
Hitomi Collaboration et al., 2016, Nature, 535, 117
Hodges-Kluck E. J., Miller M. J., Bregman J. N., 2016, ApJ, 822, 21
Hodges-Kluck E. J., Bregman J. N., Li J.-t., 2018, ApJ, 866, 126
Hodges-Kluck E. J., Yukita M., Tanner R., Ptak A. F., Bregman J. N., Li J.-t., 2020, ApJ, 903, 35
Hopkins P. F., Kereš D., Oñorbe J., Faucher-Giguère C.-A., Quataert E., Murray N., Bullock J. S., 2014, MNRAS, 445, 581
Huang R., et al., 2023a, in prep.
Huang S., Cappelluti N., Galeazzi M., Gupta A., Liu W., Ursino E., Velliyedathu T. J., 2023b, ApJ, 947, 49
Humphrey P. J., Buote D. A., 2006, ApJ, 639, 136
Irwin J., et al., 2012a, AJ, 144, 43
Irwin J., et al., 2012b, AJ, 144, 44
Jiang Y.-F., Stone J. M., Davis S. W., 2014, ApJ, 796, 106
Jiang X., Li J., Fang T., Wang Q. D., 2019, ApJ, 885, 38
Jones C., Forman W., 1984, ApJ, 276, 38
Kaaret P., et al., 2020, Nature Astronomy, 4, 1072
Kallman T., Bautista M., 2001, ApJS, 133, 221
Kam S. Z., Carignan C., Chemin L., Foster T., Elson E., Jarrett T. H., 2017, AJ, 154, 41
Kara E., Dai L., Reynolds C. S., Kallman T., 2018, MNRAS, 474, 3593
Kereš D., Katz N., Weinberg D. H., Davé R., 2005, MNRAS, 363, 2
Kim D.-W., Fabbiano G., 2015, ApJ, 812, 127
Kim C.-G., Ostriker E. C., 2018, ApJ, 853, 173
Kim D.-W., et al., 2019, ApJS, 241, 36
Kochanek C. S., 2016, MNRAS, 458, 127
Krause M., et al., 2020, A&A, 639, A112
Krishnarao D., et al., 2022, Nature, 609, 915
Lehner N., Howk J. C., 2011, Science, 334, 955
Lehner N., Howk J. C., Wakker B. P., 2015, ApJ, 804, 79

Lehner N., et al., 2020, ApJ, 900, 9
Leroy A. K., et al., 2009, AJ, 137, 4670
Li J.-T., 2015, MNRAS, 453, 1062
Li J.-T., 2020, Astronomische Nachrichten, 341, 177
Li J.-T., Wang Q. D., 2013a, MNRAS, 428, 2085
Li J.-T., Wang Q. D., 2013b, MNRAS, 435, 3071
Li Z., Wang Q. D., Irwin J. A., Chaves T., 2006, MNRAS, 371, 147
Li Z., Wang Q. D., Hameed S., 2007, MNRAS, 376, 960
Li J.-T., Li Z., Wang Q. D., Irwin J. A., Rossa J., 2008, MNRAS, 390, 59
Li J.-T., Wang Q. D., Li Z., Chen Y., 2009, ApJ, 706, 693
Li J.-T., Crain R. A., Wang Q. D., 2014, MNRAS, 440, 859
Li J.-T., et al., 2016a, MNRAS, 456, 1723
Li J.-T., Decourchelle A., Miceli M., Vink J., Bocchino F., 2016b, MNRAS, 462, 158
Li J.-T., Bregman J. N., Wang Q. D., Crain R. A., Anderson M. E., 2016c, ApJ, 830, 134
Li J.-T., Bregman J. N., Wang Q. D., Crain R. A., Anderson M. E., Zhang S., 2017a, ApJS, 233, 20
Li J.-T., Bregman J. N., Wang Q. D., Crain R. A., Anderson M. E., Zhang S., 2017b, ApJS, 233, 20
Li J.-T., Bregman J. N., Wang Q. D., Crain R. A., Anderson M. E., 2018, ApJL, 855, L24
Li J.-T., Hodges-Kluck E., Stein Y., Bregman J. N., Irwin J. A., Dettmar R.-J., 2019, ApJ, 873, 27
Li Y., et al., 2020, ApJL, 889, L1
Li J.-T., et al., 2022, MNRAS, 515, 2483
Lin D., et al., 2015, ApJ, 811, 43
Lin D., et al., 2018, Nature Astronomy, 2, 656
Liu J., Mao S., Wang Q. D., 2011, MNRAS, 415, L64
Liu J., Wang Q. D., Mao S., 2012, MNRAS, 420, 3389
Liu F. K., Li S., Komossa S., 2014, ApJ, 786, 103
Lockman F., Betti S. K., Hill A. S., Lehner N., Shelton R. L., Wakker B. P., 2019, BAAS, 51, 255
Lodato G., Franchini A., Bonnerot C., Rossi E. M., 2015, Journal of High Energy Astrophysics, 7, 158
Lopez L. A., Mathur S., Nguyen D. D., Thompson T. A., Olivier G. M., 2020, ApJ, 904, 152
Lu W., Kumar P., 2018, ApJ, 865, 128
Luo Y., Fang T., Ma R., 2018, ApJS, 235, 28
Mac Low M.-M., McCray R., Norman M. L., 1989, ApJ, 337, 141
Machacek M. E., Jones C., Forman W. R., 2004, ApJ, 610, 183
Maller A. H., Bullock J. S., 2004, MNRAS, 355, 694
Mao J., et al., 2021, ApJL, 918, L17
Marinacci F., Binney J., Fraternali F., Nipoti C., Ciotti L., Londrillo P., 2010, MNRAS, 404, 1464
McCammon D., et al., 2002, ApJ, 576, 188
McGaugh S. S., Schombert J. M., de Blok W. J. G., Zagursky M. J., 2010, ApJL, 708, L14
Melioli C., Brighenti F., D'Ercole A., 2015, MNRAS, 446, 299
Ménard B., Scranton R., Fukugita M., Richards G., 2010, MNRAS, 405, 1025
Metzger B. D., Stone N. C., 2016, MNRAS, 461, 948
Miller M. J., Bregman J. N., 2013, ApJ, 770, 118
Miller M. J., Bregman J. N., 2015, ApJ, 800, 14
Miller J. M., et al., 2015, Nature, 526, 542
Mou G., et al., 2023, Nature Communications, 14, 781
Mushotzky R., 2018, in den Herder J.-W. A., Nikzad S., Nakazawa K., eds, Society of Photo-Optical Instrumentation Engineers (SPIE) Conference Series Vol. 10699, Space Telescopes and Instrumentation 2018: Ultraviolet to Gamma Ray. p. 1069929 (arXiv:1807.02122), doi:10.1117/12.2310003
Nakashima S., Inoue Y., Yamasaki N., Sofue Y., Kataoka J., Sakai K., 2018, ApJ, 862, 34
Nelson D., et al., 2020, MNRAS, 498, 2391
Noutsos A., 2012, SSRv, 166, 307
O'Sullivan E., Ponman T. J., Collins R. S., 2003, MNRAS, 340, 1375
Ogle P. M., Lanz L., Nader C., Helou G., 2016, ApJ, 817, 109
Oosterloo T., Fraternali F., Sancisi R., 2007, AJ, 134, 1019
Oppenheimer B. D., 2018, MNRAS, 480, 2963
Peek J. E. G., Bordoloi R., Sana H., Roman-Duval J., Tumlinson J., Zheng Y., 2016, ApJL, 828, L20
Peeples M. S., Werk J. K., Tumlinson J., Oppenheimer B. D., Prochaska J. X., Katz N., Weinberg D. H., 2014, ApJ, 786, 54
Pillepich A., Nelson D., Truong N., Weinberger R., Martin-Navarro I., Springel V., Faber S. M., Hernquist L., 2021, MNRAS, 508, 4667
Piran T., Svirski G., Krolik J., Cheng R. M., Shiokawa H., 2015, ApJ, 806, 164
Ponman T. J., Bourner P. D. J., Ebeling H., Böhringer H., 1996, MNRAS, 283, 690
Ponti G., et al., 2023, A&A, 674, A195
Predehl P., et al., 2020, Nature, 588, 227
Predehl P., et al., 2021, A&A, 647, A1
Prochaska J. X., Zheng Y., 2019, MNRAS, 485, 648
Prochaska J. X., et al., 2019, Science, 366, 231
Putman M. E., Peek J. E. G., Joung M. R., 2012, ARA&A, 50, 491

Qu Z., Bregman J. N., 2018, ApJ, 856, 5
Qu Z., Bregman J. N., Hodges-Kluck E., Li J.-T., Lindley R., 2020, ApJ, 894, 142
Qu Z., Huang R., Bregman J. N., Li J.-T., 2021, ApJ, 907, 14
Qu Z., Koutroumpa D., Bregman J. N., Kuntz K. D., Kaaret P., 2022, ApJ, 930, 21
Ramesh R., Nelson D., Pillepich A., 2023, MNRAS, 522, 1535
Rao S. M., Sardane G., Turnshek D. A., Thilker D., Walterbos R., Vanden Berk D., York D. G., 2013, MNRAS, 432, 866
Rasmussen A., Kahn S. M., Paerels F., 2003, in Rosenberg J. L., Putman M. E., eds, Astrophysics and Space Science Library Vol. 281, The IGM/Galaxy Connection. The Distribution of Baryons at z=0. p. 109 (arXiv:astro-ph/0301183), doi:10.1007/978-94-010-0115-1_20
Rasmussen J., Sommer-Larsen J., Pedersen K., Toft S., Benson A., Bower R. G., Grove L. F., 2009, ApJ, 697, 79
Raymond J. C., Smith B. W., 1977, ApJS, 35, 419
Rees M. J., 1988, Nature, 333, 523
Revnivtsev M., Churazov E., Sazonov S., Forman W., Jones C., 2007a, A&A, 473, 783
Revnivtsev M., Vikhlinin A., Sazonov S., 2007b, A&A, 473, 857
Revnivtsev M., Churazov E., Sazonov S., Forman W., Jones C., 2008, A&A, 490, 37
Richardson J. C., et al., 2011, ApJ, 732, 76
Rossa J., Dettmar R. J., 2003, A&A, 406, 493
Rupke D. S. N., et al., 2019, Nature, 574, 643
Ruszkowski M., Yang H. Y. K., Reynolds C. S., 2017, ApJ, 844, 13
Sancisi R., Fraternali F., Oosterloo T., van Moorsel G., 2001, in Funes J. G., Corsini E. M., eds, Astronomical Society of the Pacific Conference Series Vol. 230, Galaxy Disks and Disk Galaxies. pp 111–118 (arXiv:astro-ph/0010407), doi:10.48550/arXiv.astro-ph/0010407
Sazonov S., et al., 2021, MNRAS, 508, 3820
Schaye J., et al., 2015, MNRAS, 446, 521
Schmelz J. T., Verschuur G. L., 2023, ApJ, 943, 44
Sembach K. R., et al., 2003, ApJS, 146, 165
Seward F. D., Forman W. R., Giacconi R., Griffiths R. E., Harnden F. R. J., Jones C., Pye J. P., 1979, ApJL, 234, L55
Shapiro P. R., Field G. B., 1976, ApJ, 205, 762
Shelton R. L., Kwak K., Henley D. B., 2012, ApJ, 751, 120
Sheng Z., Wang T., Ferland G., Shu X., Yang C., Jiang N., Chen Y., 2021, ApJL, 920, L25
Shu X., et al., 2020, Nature Communications, 11, 5876
Shull J. M., Jones J. R., Danforth C. W., Collins J. A., 2009, ApJ, 699, 754
Silich S., Tenorio-Tagle G., Añorve-Zeferino G. A., 2005, ApJ, 635, 1116
Smith R. K., Foster A. R., Brickhouse N. S., 2012, Astronomische Nachrichten, 333, 301
Snowden S. L., et al., 1995, ApJ, 454, 643
Snowden S. L., et al., 1997, ApJ, 485, 125
Sobey C., et al., 2019, MNRAS, 484, 3646
Stevens I. R., Read A. M., Bravo-Guerrero J., 2003, MNRAS, 343, L47
Strickland D. K., Heckman T. M., 2009, ApJ, 697, 2030
Strickland D. K., Stevens I. R., 2000, MNRAS, 314, 511
Strickland D. K., Heckman T. M., Weaver K. A., Hoopes C. G., Dahlem M., 2002, ApJ, 568, 689
Strickland D. K., Heckman T. M., Colbert E. J. M., Hoopes C. G., Weaver K. A., 2004a, ApJS, 151, 193
Strickland D. K., Heckman T. M., Colbert E. J. M., Hoopes C. G., Weaver K. A., 2004b, ApJ, 606, 829
Strubbe L. E., Quataert E., 2011, MNRAS, 415, 168
Sun M., Voit G. M., Donahue M., Jones C., Forman W., Vikhlinin A., 2009, ApJ, 693, 1142
Sutherland R. S., Dopita M. A., 1993, ApJS, 88, 253
Tamm A., Tempel E., Tenjes P., Tihhonova O., Tuvikene T., 2012, A&A, 546, A4
Tang S., Wang Q. D., Lu Y., Mo H. J., 2009, MNRAS, 392, 77
Thom C., Peek J. E. G., Putman M. E., Heiles C., Peek K. M. G., Wilhelm R., 2008, ApJ, 684, 364
Toft S., Rasmussen J., Sommer-Larsen J., Pedersen K., 2002, MNRAS, 335, 799
Townsley L. K., Feigelson E. D., Montmerle T., Broos P. S., Chu Y.-H., Garmire G. P., 2003, ApJ, 593, 874
Tripp T. M., Song L., 2012, ApJ, 746, 173
Tüllmann R., Pietsch W., Rossa J., Breitschwerdt D., Dettmar R. J., 2006a, A&A, 448, 43
Tüllmann R., Breitschwerdt D., Rossa J., Pietsch W., Dettmar R. J., 2006b, A&A, 457, 779
Tumlinson J., et al., 2011, Science, 334, 948
Tumlinson J., Peeples M. S., Werk J. K., 2017, ARA&A, 55, 389

Vargas C. J., Walterbos R. A. M., Rand R. J., Stil J., Krause M., Li J.-T., Irwin J., Dettmar R.-J., 2019, ApJ, 881, 26

Veilleux S., Cecil G., Bland-Hawthorn J., 2005, ARA&A, 43, 769

Veilleux S., Rupke D. S. N., Swaters R., 2009, ApJL, 700, L149

Veilleux S., Maiolino R., Bolatto A. D., Aalto S., 2020, A&A Rv, 28, 2

Vijayan A., Li M., 2022, MNRAS, 510, 568

Vogelsberger M., et al., 2014, MNRAS, 444, 1518

Voit G. M., Donahue M., 2015, ApJL, 799, L1

Voit G. M., Donahue M., Bryan G. L., McDonald M., 2015, Nature, 519, 203

Wakker B. P., Savage B. D., 2009, ApJS, 182, 378

Wakker B. P., et al., 1999, Nature, 402, 388

Wakker B. P., et al., 2007, ApJL, 670, L113

Wakker B. P., York D. G., Wilhelm R., Barentine J. C., Richter P., Beers T. C., Ivezić Ž., Howk J. C., 2008, ApJ, 672, 298

Walter F., Brinks E., de Blok W. J. G., Bigiel F., Kennicutt Robert C. J., Thornley M. D., Leroy A., 2008, AJ, 136, 2563

Wang Q. D., 2010, Proceedings of the National Academy of Science, 107, 7168

Wang Q. D., Liu J., 2012, Astronomische Nachrichten, 333, 373

Wang Q. D., et al., 2005, ApJ, 635, 386

Wang Q. D., Li J., Jiang X., Fang T., 2016, MNRAS, 457, 1385

Weaver R., McCray R., Castor J., Shapiro P., Moore R., 1977, ApJ, 218, 377

Werk J. K., et al., 2014, ApJ, 792, 8

Westmeier T., 2018, MNRAS, 474, 289

Whaley C. H., Irwin J. A., Madden S. C., Galliano F., Bendo G. J., 2009, MNRAS, 395, 97

White S. D. M., Frenk C. S., 1991, ApJ, 379, 52

Wolk S. J., Bourke T. L., Smith R. K., Spitzbart B., Alves J., 2002, ApJL, 580, L161

Wulf D., et al., 2019, ApJ, 884, 120

Yang C., Wang T., Ferland G. J., Dou L., Zhou H., Jiang N., Sheng Z., 2017, ApJ, 846, 150

Yao Y., Wang Q. D., 2005, ApJ, 624, 751

Yao Y., et al., 2023, arXiv e-prints, p. arXiv:2303.06523

Young J. S., et al., 1995, ApJS, 98, 219

Yuan W., et al., 2018, in den Herder J.-W. A., Nikzad S., Nakazawa K., eds, Society of Photo-Optical Instrumentation Engineers (SPIE) Conference Series Vol. 10699, Space Telescopes and Instrumentation 2018: Ultraviolet to Gamma Ray. p. 1069925, doi:10.1117/12.2313358

Zhang D., Thompson T. A., Murray N., Quataert E., 2014a, ApJ, 784, 93

Zhang S., Wang Q. D., Ji L., Smith R. K., Foster A. R., Zhou X., 2014b, ApJ, 794, 61

Zhang D., Thompson T. A., Quataert E., Murray N., 2017, MNRAS, 468, 4801

Zhang Y.-N., Li C., Xu D., Cui W., 2022a, Experimental Astronomy, 53, 1053

Zhang S., Wang Q. D., Sun W., Long M., Sun J., Ji L., 2022b, ApJ, 941, 68

Zheng Y., et al., 2022, Research in Astronomy and Astrophysics, 22, 085004

Zhuravleva I., et al., 2014, Nature, 515, 85

van Velzen S., et al., 2021, ApJ, 908, 4